NOVA SCHOOL OF SCIENCE & TECHNOLOGY

DEPARTMENT OF MATERIALS SCIENCE

DIOGO GONÇALO ALVES CASTANHEIRA

BSc of Science in Micro and Nanotechnology Engineering

Fourier microscopy for the characterization of plasmonic solar cells

MSc of Micro and Nanotechnology Engineering

NOVA School of Science and Technology

October, 2022

NOVA SCHOOL OF SCIENCE & TECHNOLOGY

DEPARTAMENT OF MATERIALS SCIENCE

Fourier microscopy for the characterization of plasmonic solar cells

DIOGO GONÇALO ALVES CASTANHEIRA

BSc of Science in Micro and Nanotechnology Engineering

Adviser: Dr. Jaime Gómez Rivas
Full Professor, Eindhoven University of Technology

Co-advisers: Dr. Manuel Mendes
Assistant Professor, NOVA University Lisbon

Examination Committee:

Chair: Hugo Águas,
Assistant Professor, NOVA University Lisbon

Rapporteurs: Matthijs Berghuis,
Ph.D. Student, Eindhoven University of Technology

Members: Jaime Gómez Rivas,
Full Professor, Eindhoven University of Technology

MASTER OF SCIENCE IN MICRO AND NANOTECHNOLOGY ENGINEERING

NOVA University Lisbon
October, 2022

Fourier microscopy for the characterization of plasmonic solar cells

ACKNOWLEDGMENTS

First and foremost, I would like to thank my daily mentor during this thesis Saad, and my supervisor Jaime, for accepting me and allowing the development of this work, and for all the knowledge and mentorship, all the patience and guidance throughout this journey. You guys were amazing. I would also like to thank the PSN group at TU/e, where this thesis was conducted, as they are such amazing people - which allowed a great work environment. A special thanks to Matthijs, Ping and Lian for all the help provided and knowledge shared. The work ethic and the friendship bonds of the group allows for an incredible environment to work in, that I very much appreciated.

I also need to thank professor Manuel Mendes not only for his availability to help me during this thesis, but also for being a great professor and an inspiration for me and many students.

I want to thank all my hometown friends. To Alex, Bruno, Edu, Luís, Marcelo, Pacau, PP, Ramalho, Tomás, Tomé, and Zé: thank you for all the great moments during so many years. May the group SARDAS live forever.

I also want to thank Mariana for all the support and moments shared together throughout the years.

To Ricardo, and António da Cruz, two friendships that never ended throughout the years even though we were not able to see each other for most of that time, my big thank you.

To my first flatmate Miguel - which lived with me during our first three years of university - for all the good and bad moments that we went through together, my big thank you.

To Mariana Felipa de Erasmus, Bia, Inês Diogo, Maria and Tomás: these five university years would not have been the same without you all. I will miss studying and partying with you at FCT/UNL.

Lastly, my big thanks from the bottom of my heart to my amazing parents and sister, for all the support, guidance, and love.

And to you, António.

“Enjoying the beauty, I lived as I wanted.”
(Matsuo Bashō)

ABSTRACT

The recent advances in different fields regarding nanomaterials and plasmonic devices urge for the improvement and development of new high accuracy tools for their characterization. Among those devices are plasmonic solar cells with metallic nanoparticles embedded on their composition. Those cells have been a recurrent topic of research in the scientific community due to their unique properties derived from the interactions of the particles with the incident light. Due to their size and physical properties, those cells and similar devices, could benefit from a time and cost-efficient method to measure their properties under different illumination angles. Therefore, this thesis proposes a Fourier optical setup based on lenses and microscopy principles to characterize plasmonic solar cells. The current given by the cells under different illumination angles is studied aiming to understand the impact of metallic nanoparticles with different sizes and spacing in a bulk heterojunction organic solar cell. Furthermore, to support those measurements, simulations are performed with different software packages, namely Lumerical, MATLAB and COMSOL. The proper alignment of the optical setup is thereby explained in detail, as well as its characterization. Ultimately, it is shown that the setup is reliable, although the solar cells studied do not seem to benefit from the illumination under different incident angles.

Keywords: Microscopy; Fourier; Solar cells; Illumination angle dependency.

RESUMO

Os recentes avanços em diferentes áreas relacionadas com nanomateriais e dispositivos plasmónicos exigem o aprimoramento e desenvolvimento de novas ferramentas de alta precisão para a sua caracterização. Entre esses dispositivos estão células solares plasmónicas com nanopartículas metálicas embutidas na sua composição. Este tipo de células tem sido um tema recorrente de pesquisa na comunidade científica devido às suas propriedades únicas derivadas das interações das partículas com a luz incidente. Devido ao seu tamanho e propriedades físicas, essas células e outros dispositivos semelhantes, podem beneficiar de um método barato e eficiente para medir as suas propriedades sob diferentes ângulos de iluminação. Esta tese propõe assim uma setup ótica de Fourier baseada nos princípios físicos de lentes e de microscopia, para caracterizar células solares plasmónicas. A corrente produzida pelas células sob diferentes ângulos de iluminação é estudada com o objetivo de entender o impacto de nanopartículas metálicas com diferentes tamanhos e espaçamento entre si, em uma célula solar orgânica de heterojunção. Além disso, são realizadas simulações com diferentes softwares, nomeadamente Lumerical, MATLAB e COMSOL. O alinhamento da setup ótica é explicado em detalhe, assim como a sua caracterização. Por fim, é demonstrado que a configuração é confiável, embora as células solares estudadas não beneficiem com diferentes ângulos de iluminação.

Palavras-chave: Microscopia; Fourier; Células solares; Dependência de ângulo de iluminação.

CONTENTS

LIST OF FIGURES

ACRONYMS

BFP	Back focal plane
CCD	Charge-coupled device
OSCs	Organic solar cells
HOMO	Highest occupied molecular orbital
LUMO	Lowest unoccupied molecular orbital
ETL	Electron transport layer
HTL	Hole transport layer
PCE	Power-conversion efficiency
FDTD	Finite-Difference Time-Domain
TMM	Transfer matrix method
BS	Beam splitter
NA	Numerical aperture
TM	Transverse magnetic
TE	Transverse electric
PSN	Photonics and Semiconductor Nanophysics

SYMBOLS

Symbol	Name	Unit
$\boldsymbol{Ag}$	Silver	
$\boldsymbol{Au}$	Gold	
$\boldsymbol{d}$	Spacing between grooves	nm
$\boldsymbol{d_i}$	Projected image distance	m
$\boldsymbol{d_o}$	Projected object distance	m
$\boldsymbol{e}$	Electron charge	
$\boldsymbol{\|E\|^2}$	Electric field intensity	$(V/m)^2$
$\boldsymbol{f}$	Focal distance	mm
$\boldsymbol{F}$	Focal point	
$\hbar$	Planck's constant	$kg\,.m^2.s^{-2}$
$\boldsymbol{I}$	Current	A
$\boldsymbol{I_{AM1.5}}$	AM1.5 irradiance spectrum	W/m^2nm
$\boldsymbol{ITO}$	Indium tin oxide	
$\boldsymbol{J_{SC}}$	Short circuit current density	mA/cm^2
$\boldsymbol{k}$	Wave vector	1/nm
$\boldsymbol{MoO_3}$	Molybdenum trioxide	
$\boldsymbol{n}$	Refractive index	
$\boldsymbol{n_d}$	Order of diffraction	
$\boldsymbol{P}$	Pitch size	nm
$\boldsymbol{Si}$	Silicon	
$\boldsymbol{\omega}$	Angular frequency	rad/s
$\boldsymbol{ZnO}$	Zinc oxide	
$\boldsymbol{\theta}$	Theta	º
$\boldsymbol{\varphi}$	Phi	º
$\boldsymbol{\lambda}$	Light wavelength	nm
Δ_0	Maximum thickness of a lens	Nm

1 INTRODUCTION

The motivation for the present work is depicted in this chapter. Some optical fundamentals regarding convex lenses will be explained as they play a major role on the Fourier microscopy setup that was built during this thesis. An introduction to bulk heterojunction organic solar cells is also given, as those will be the type of devices that will be studied both with simulations and experimental data.

1.1 Motivation

Multiple software can be used to simulate directional light emission and absorption by different types of nanoscale devices, such as Lumerical, COMSOL or MATLAB. Although, for experimental measurements, this can become a tricky thing to do due to the small scale of the devices and the high precision requirements.

Precise rotational stages - often called goniometers - are typically used to measure directional optical properties of large-area samples [1]–[5]. In this type of measurement, light that is emitted or scattered by the sample in a particular direction can be collected by a detector which can be precisely rotated around the sample. In some cases the detector can only rotate in one plane, and some of the light reflected/scattered by the sample might not be fully collected and analyzed. Considering the limitations of rotation stage-based techniques, microscopy has become a usual method for directional light measurements.

Among the wide range of microscopy techniques used by the scientific community, Fourier microscopy has been widely used for measurements of directional light emission in nanoscale samples. This technique is directly related to the optical properties of lenses, that can focus plane waves on unique positions in their back focal plane which contains information about the light intensity scattered/emitted in particular directions [6], [7]. This so-called Fourier image represents information on the reciprocal space, while the input image is the spatial domain equivalent. Fourier microscopy has been used for imaging the directional emission of fluorescent beads [8], dye-molecules coupled to plasmonic gratings [9], quantum dots coupled to plasmon antennas [10] or single plasmonic nanowires [11], [12].

In this thesis an optical setup is described, which, in similarity with a Fourier microscope, makes use of the back focal plane of an objective lens. However, this setup does not aim to make direct measurements from the Fourier image – instead, it will make use of the optical properties of lenses and the objective to redirect light onto samples with different (and controllable) illumination angles. The short-circuit current density (J_{SC}) of solar cells with metallic nanoparticles embedded in their composition is studied in this thesis.

The standard characterizations for commercial photovoltaic are performed at normal incidence, although these are not sufficient to evaluate the overall cell efficiency during the day, since the rotation of the earth and the diffuse component of solar radiation may represent a considerable percentage to take into account [13], [14], [15]. By having nanoparticles, light might have different interactions inside the devices, and thus it might present higher J_{SC} values for certain angles of illumination.

1.1.1 Lenses theory and introduction to Fourier microscopy

Microscopy techniques are mainly based on the optical properties of lenses, which can have many shapes and different properties [16], [17], [18]. For the purpose of this work, only convex lenses made of glass (n = 1.5) were considered. These convex lenses can be easily identified by their shape, whereas they have a thick mid cross section in comparison to its thinner upper and lower edges. When parallel rays of light pass

through a convex lens, the refracted rays converge at a single point F, at a focal distance f of the lens on the other side of the plane of light emission, as depicted on Figure 1.

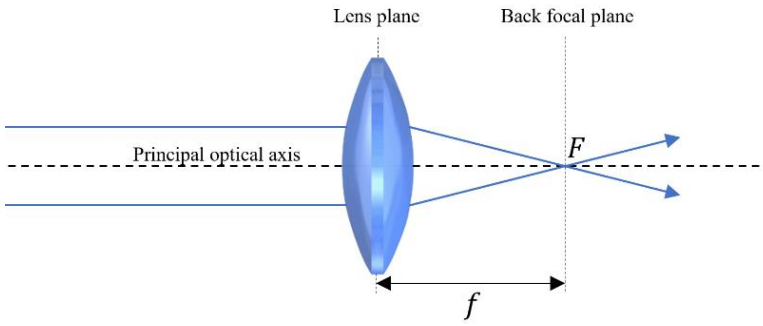

Figure 1 - Ray tracing schematic for a convex lens hit by a collimated light beam.

The same principle can be observed in an inverse and reciprocal way, whereas if the light rays of an emission source converge at exactly the focal distance of a convex lens, they will diverge until hitting the lens and then get refracted parallel to the optical axis in such a way that it is considered that the focus will be at infinity (at the rear side of the lens, considering the illumination source the front side).

The XY plane where the focal distance of a lens sits is called the focal plane. When the lens is moved on its XY plane, the focus point of an incident light beam will also be displaced on the focal plane (Figure 2)[19]. The same happens if the lens is at a fixed position but the incident beam is displaced and hits the lens at a different position.

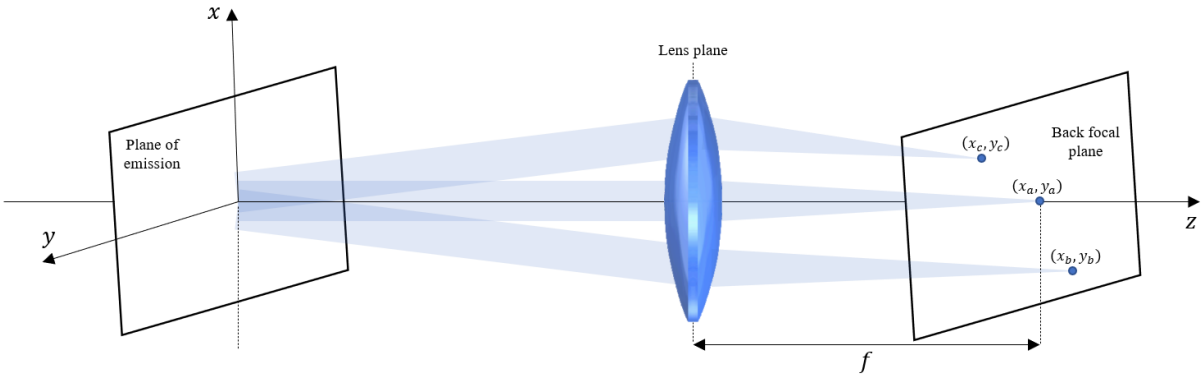

Figure 2 - Ray tracing schematic for a fixed convex lens where there is a displacement of the incident beam which creates a displacement on the back focal plane of the lens.

This can be described by the transmittivity of a lens, giving the relation between an incoming wave with an amplitude distribution $U_i(\xi,\eta)$ and the transmitted wave with an amplitude distribution $U_t(\xi,\eta)$, where (ξ,η) are the coordinates in the plane of the lens [20], [21], [22]. This relation is given by:

$$U_t(\xi,\eta) = \mathrm{t}(\xi,\eta) \cdot U_i(\xi,\eta), \tag{1}$$

where the transmittivity of a converging spherical lens $\mathrm{t}(\xi,\eta)$ is given by:

$$\mathrm{t}(\xi,\eta) = e^{(ikn\Delta_0)} e^{\left(-i\frac{k}{2f}(\xi^2+\eta^2)\right)}, \tag{2}$$

where k represents the wavenumber ($k = \frac{2\pi}{\lambda}$, where λ is the wavelength of the incident light), and Δ_0 the maximum thickness of the lens. The amplitude at a distance f from the lens is then given as a function of the incident field amplitude $U_i(\xi, \eta)$, considering the Fresnel diffraction integral which describes the propagation of waves:

$$U_f(x, y) = \frac{e^{(i\frac{k}{2f}(x^2+y^2))}}{i\lambda f} \iint_{-\infty}^{+\infty} U_i(\xi, \eta)\, e^{\left(-i\frac{2\pi}{\lambda f}(\xi x+\eta y)\right)} \mathrm{d}\xi \mathrm{d}\eta, \tag{3}$$

where x and y represent the spatial coordinates in the focal plane of a lens.

The focal plane at the rear side of the lens in respect to the plane of illumination is called the back focal plane (BFP). In this thesis a Fourier microscopy setup is used. This type of microscope makes use of the properties of the BFP as it provides an alternative set of information which is not available in conventional real space imaging, whereas in this plane the information is encoded in angular co-ordinates in contrast to the real plane image, where the resolution is in spatial coordinates. Placing a screen/detector in the BFP reveals an intensity map of the directional scattering/emission referred to as a Fourier image. This plane has emerged as an important tool for nanophotonics. Measuring the angular emission pattern has been utilized in several applications, such as measuring radiation patterns from nanoantennas [23], in understanding coupling mechanisms in cavities [24], and much more.

A conventional microscope makes use of real-space imaging, which means that the object being studied is projected as an image trough a set of lenses at some point of the optical path. A simple explanation for this real image formation is thoroughly explained in any optics book [6], [22]. Making use of a simple convex lens is the most practical example, which can be described by an algebraic relationship that relates the focal length to the distance of the object to the lens, and the distance of the correspondent projected image on the opposite side of the lens, given by

$$\frac{1}{f} = \frac{1}{d_o} + \frac{1}{d_i} \tag{4}$$

where d_o is the object distance and d_i the projected image distance.

Making use of the properties of lenses described above, a Fourier microscopy setup was built and aligned in this thesis, with the goal of understanding how different incident light angles would affect the J_{SC} of plasmonic solar cells. This setup will make use of both real-space and Fourier space imaging for the proper alignment of the components used, and for the characterization of the results obtained. It makes use of real-space imaging in a $2f$ configuration, where a lens is placed at the middle point of the optical path between a CCD (charge-coupled device) camera and an imaging plane (a projection of the object), at a distance of $2f$ from each. As for Fourier imaging, the distance between the object and the lens is trivial and depends only on the directionality of the emission, as long as the detector – in this case, another CCD camera – is placed at the BFP of the lens, although for simplicity, a $1f$ configuration was used. A schematic of the configuration explained above is thereby presented on Figure 3, which resembles the lenses configuration that will be used on the setup.

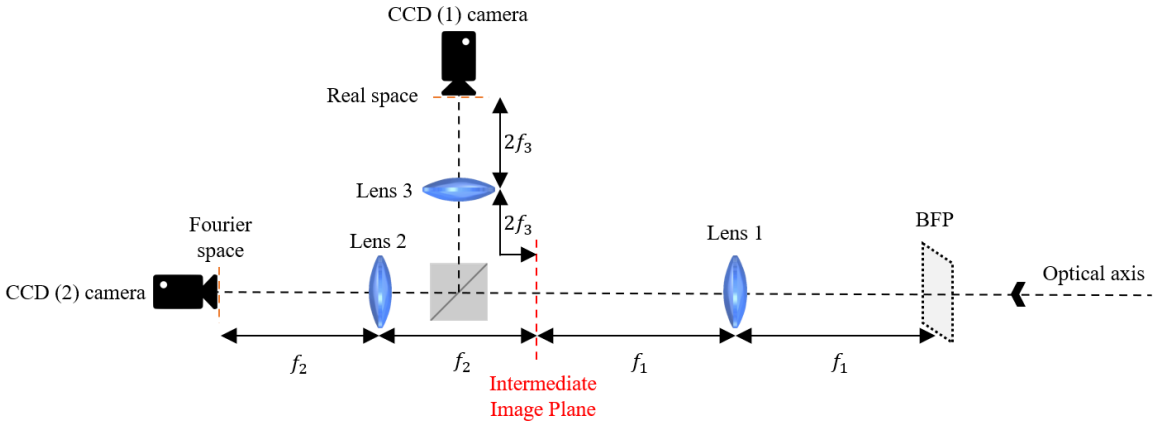

Figure 3 - Schematic of the lenses configuration used on the Fourier setup.

1.2 Bulk heterojunction organic solar cells

The world energy consumption has been increasing exponentially since the industrial revolution, in response to modern living standards, that are leading to a continuous expansion of daily production and energy demand. However, the availability of primary exhaustible energy sources such as fossil fuels and uranium, and the long-term adverse effects on the environment due to their exploitation, reflects on the urgency to develop new strategies to effectively utilize other primary energy sources: the renewable ones [25]. Solar power has the potential to replace these exhaustible energy sources, although the majority of commercial solar cells is based on silicon (Si), and even though the production costs have dropped significantly over the past decades, the record efficiency has only increased by 24% to 26.7% in the last two decades [26].

Organic solar cells (OSCs) based on bulk heterojunctions are promising candidates for renewable energy sources thanks to their advantages compared to inorganic solar cells, such as low-cost, lightweight, and mechanical flexibility [27]–[29]. In these devices, the active layer is made of a junction of a donor and acceptor material, whereas the donor is more electron rich (Figure 3).

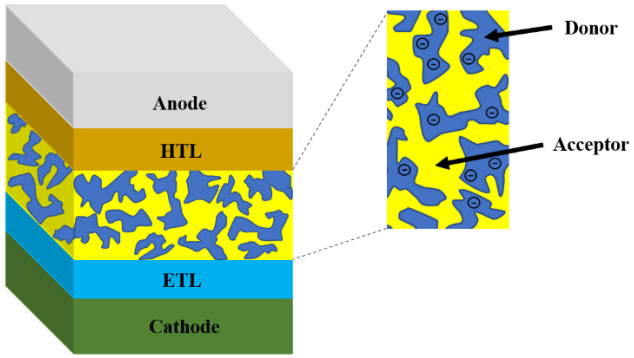

Figure 4 – Device architecture of a bulk heterojunction solar cell. A close-up of the blend (heterojunction) layer is depicted on the right.

Upon absorption of light, an electron in this active layer is excited from the highest occupied molecular orbital (HOMO) to the lowest unoccupied molecular orbital (LUMO), which will generate an electron-hole pair also known as exciton. To break up the exciton and create free charge-carriers, an electric field of energy greater than the binding energy of the electron-hole pair is required. The electric field present at the heterojunction interface allows for the dissociation of excitons into electrons and holes which can then be transported through the electron transport layer (ETL) and hole transport layer (HTL) to the electrodes at the top and

bottom sides of the device. The charge collection at the respective electrodes concludes the steps from absorption of light to generation of photocurrent.

Significant progress has been made on OSCs processing, device configuration, and film morphology to achieve high power-conversion efficiencies (PCE). However, organic materials have several drawbacks that impact the overall performance of the cell, and thus, OSCs need to be improved to be competitive with current market technologies. As an example, one of the major drawbacks that organic materials face when used in solar cells, is the relatively low carrier mobilities and short exciton-diffusion lengths, of around 100 nm, which limits the light absorption and the energy conversion efficiencies [30], [31].

Many efforts have been made to improve the PCE in OSCs by increasing the J_{SC} [32], [33], open circuit voltage [34]–[36], or extending the absorption spectrum [37]. Implementing light trapping mechanisms on these organic devices has attracted a lot of attention in recent years, as it can enable physically thin devices with high optical absorption [38]–[40]. Light absorption can then be improved by implementing a variety of nanostructures into the solar cell, such as nanoholes and nanoparticles arrays, nanorods, etc. Due to their nanometer size, these structures can interact with light in unique ways, thereby introducing plasmonic effects in the solar cell, such as surface plasmon resonances [41]–[43], guided modes [44], [45], etc. These plasmonic light trapping mechanisms get their name due to surface plasmons created on the interface between the metallic particles and the organic semiconductor around it, which enables the collective oscillation of the conduction electrons of the metal. Up to date, gold [46], [47] and silver [48]–[50] have been the most used and studied metals for this application, although to achieve the plasmonic effect in a photovoltaic device one must optimize their size [45], shape [44], and arrangement [51] since these particles can also induce optical losses (e.g.: parasitic absorption) that can outweigh the desired effects.

Optical measurements of solar cells in literature are usually done under standard test conditions, i.e., 1000 W/m^2 irradiance at normal incidence, AM1.5 spectrum, and temperature of 25ºC [13]–[15]. These conditions normally yield the highest PCE due to the fact that solar cells under different incident light angles attain more optical losses due to reflection at their surface. Although, for plasmonic solar cells, this might not be the case, as some plasmonic effects or internal reflections caused by the nanoparticles inside the device might have a different behavior under different incident light angles. In this thesis, bulk heterojunction organic solar cells with nanoparticles embedded in the active layer will have their J_{SC} studied for different incident illumination angles, through both simulated and experimental data, retrieved from different software and the Fourier setup previously described.

2

MATERIALS AND METHODS

The design of the studied solar cells is shown in this chapter. The working principle of the Fourier microscopy setup is presented, as well as a description of its alignment. The software used for simulations can also be found here.

2.1 The samples design

Four solar cells were studied during this thesis, both in simulations and experimentally – although, for the experimental work, the cells had previously been fabricated during a different project.

Three of the solar cells have embedded metallic nanoparticles. Those devices have a conformal morphology with a corrugation due to the particles. One other cell has no metallic nanoparticles, thus being a planar device, which serves as a reference sample. A schematic representation of the investigated reference solar cell device is depicted in Figure 5 (a). This solar cell consists of a 120 nm thick layer of indium tin oxide (ITO) as a transparent cathode on top of a glass substrate, an ETL layer made of zinc oxide (ZnO) with a thickness of 40 nm, an organic blend made of PDPP5T_IEICO-4F acting as the active layer with thickness of 120 nm, an HTL layer made of 10 nm of molybdenum trioxide (MoO_3), and a silver (Ag) layer with a thickness of 100 nm acting as the anode. The other three cells have a periodic array (square lattice) of cylindrical gold (Au) nanoparticles with on top of the ITO cathode, as depicted in Figure 5 (b).

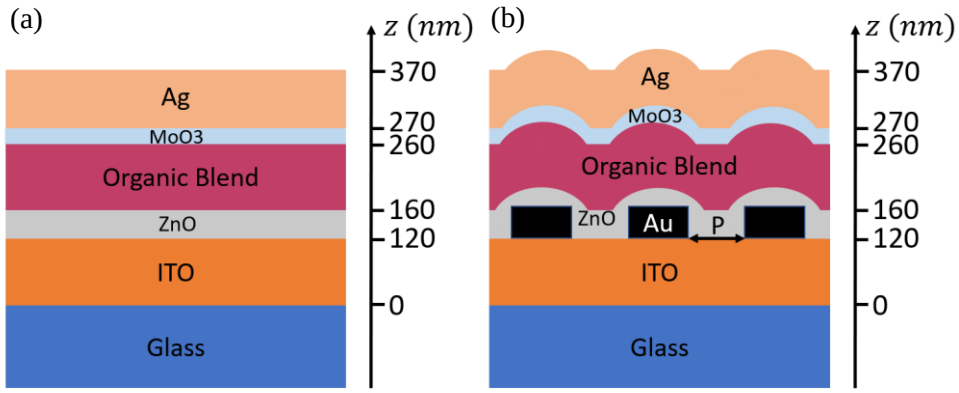

Figure 5 – Representative schematic of the (a) reference solar cell, and (b) the plasmonic solar cells studied in this thesis. Layers height and composition are depicted. The pitch size (distance between particles) is denoted with the letter "P".

The differences between these three cells are the size of the particles and the lattice constant (i.e. pitch size), as shown in Table 1. Throughout this report, the plasmonic devices – the cells with metallic nanoparticles – will be referred to by the size of their periodic array: P160 for the cell with a 160 nm lattice constant, P355 for the cell with a 355 nm lattice constant, and P420 for the cell with a 420 nm lattice constant.

	Reference – "Pref"	Sample 1 – "P160"	Sample 2 – "P355"	Sample 3 – "P420"
Particle Diameter (nm)	-	80	150	170
Pitch size (nm)	-	160	355	420
Height (nm)	-	30	30	30
Cell Side (mm)	3	3	4	4

Table 1 – Geometrical parameters of the solar cells. The "Cell Side (mm)" row refers to the size of the cells studied experimentally - although, this parameter is not relevant nor considered in the simulations.

2.2 Simulations

2.2.1 Lumerical

To describe the experimental results, optical simulations were firstly conducted employing a 3D Finite-Difference Time-Domain (FDTD) method, using the commercial software Lumerical, which solves Maxwell's equations for arbitrary geometries and materials. Since the studied devices present a periodic structure, the simulation can be simplified to a single unit cell due to the periodic condition of the device. The FDTD region was then reduced to a square unit, having the nanoparticle in the middle of the simulation region. The size of this region corresponds to the distance between two nanoparticles in each device, i.e. the lattice constant. On each side of the simulation, periodic boundary conditions were set to model the infinite periodicity of the structures. On the top and bottom sides, perfectly matched layers (PML) boundary conditions were used. A plane wave source was used to inject electromagnetic energy onto the device, to simulate the solar illumination that a real device will be exposed to. The angle at which this plane wave is injected can be stipulated, as well as the bandwidth - which had a defined value of 300-1100 nm for all the simulations.

2.2.2 COMSOL

COMSOL is a simulation software based on numerical methods. Similar to Lumerical, it can be used for plasmonic applications where the device can be designed in the workflow, and different parameters and analyses can be performed. A major advantage between this software and Lumerical is that COMSOL is a frequency domain method, which finds solutions to a proposed problem one frequency at the time, which became an important matter for achieving trustworthy results, as it will be discussed in the next section.

2.2.3 MATLAB

MATLAB is a programming platform that allows the computation, visualization, and programming of different devices. Since the simulations software previously described are time-consuming, the reference device without nanoparticles was designed and analyzed using MATLAB. For this analysis, a transfer matrix method (TMM) was applied. This method can be used to simulate different optical properties of the solar cells, by following the assumptions described by the Fresnel equations, adding the partial reflections and transmissions of a stratified medium. This software was also used to replicate data obtained by Lumerical for the plasmonic solar cells.

2.3 Experiments

In this subsection, a brief explanation of the Fourier microscopy setup and its alignment is given. Its calibration will later be discussed on the "Results and Discussion" chapter.

2.3.1 Working principle

To measure the J_{SC} provided by the solar cells at different incident light angles, a Fourier microscopy setup was designed. Its name derives from the fact that it makes use of BFP of one objective lens, also called Fourier plane, to redirect its incident light into the cells under a defined angle.

The following image (Figure 6) is a schematic of the Fourier setup built during this thesis, which includes the name of all its components, which will be broadly used throughout this report.

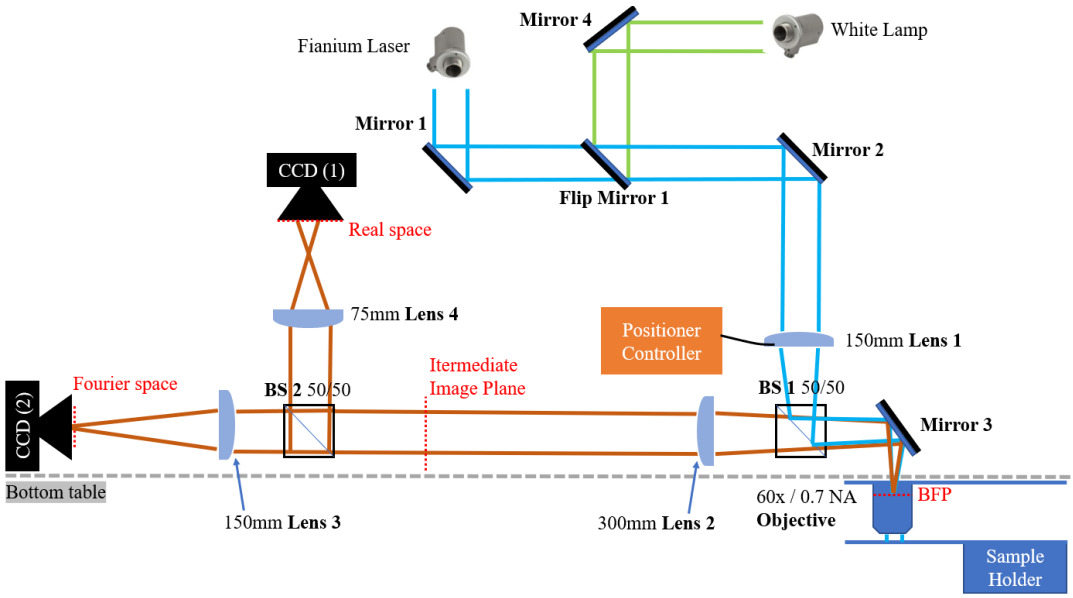

Figure 6 - Full schematic of the Fourier microscopy setup used in this thesis.

This setup makes use of two light paths: one uses a SuperK FIANIUM light laser which uses a tunable source - allowing the user to choose the desired light wavelength (400 to 1100 nm range) to be used in a specific measurement, as well as its intensity; the other light path uses a white lamp, which emits all wavelengths simultaneously (in the 400-1600 nm range). The first route (depicted in blue) is going to be used for measuring the current given by the sample at different illumination wavelengths, while the second route (depicted in green) is necessary to see the real space image of the sample in the CCD (1) camera to make sure that the sample is at the exact focal distance of the objective lens. Both light paths are guided through a set of mirrors and a beam splitter (BS 1) and are focused in the BFP of the objective by Lens 1, resulting in a collimated illumination of the samples. Those samples are placed inside a holder which is named "EQE box" (Appendix 4). This sample holder is mounted to a 3D stage that can have its position manually controlled in all XYZ coordinates through millimetric screws. The EQE box has four coaxial pins (one for each cell – that connect to the cathode and anode) that can be connected to a coaxial cable that leads into a multimeter that measures the current produced by each sample. The light reflected back from the sample is collimated by Lens 2 - which needs to be placed at the focal distance of the objective used – and it hits both CCD cameras through the use of another beam splitter (BS 2), and two lenses (Lens 3 and Lens 4) that focus the beam. Both cameras are connected to a computer, where the user is able to see the real space image of the sample, given by CCD (1), and the Fourier space, given by CCD (2). In order to excite the sample at different angles, Lens 1 can be

moved using electrical motors. Due to this movement the beam hits Lens 1 slightly off-center, resulting in a displacement of the focus point the back focal plane of the objective, which will then excite the sample with different angles [52](Figure 7).

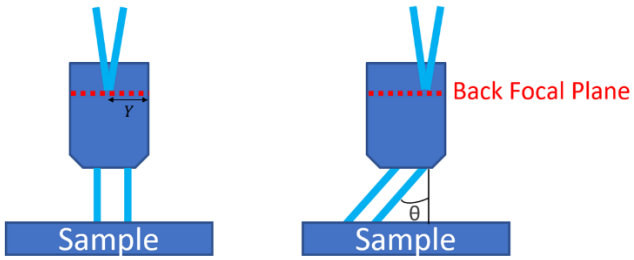

Figure 7 - Representation of how the beam position on the BFP of the objective changes the angle of illumination on the sample.

This assumption can easily be proven visually by seeing the beam coming out of the objective being shifted when moving Lens 1. It can also be explained by mathematical methods, considering the optical properties of the objective used in the measurements. When the beam hits the center of the BFP of the objective, it does not get displaced and hits the cell at a 0º (normal incidence). When changing the position of the beam on the BFP, the incident angle on the cell changes accordingly. To understand this correlation, one must consider the numerical aperture (NA) of the objective lens used, which is indicated by the manufacturer, and defines the maximum angle of incidence when focusing light, as well as the maximum angle of light collection when detecting light. The NA can be calculated with the formula:

$$NA = n \sin(\theta_{MAX}), \tag{5}$$

where n is the refractive index of the medium between the objective lens and the sample ($n \cong 1$ for air), and θ_{MAX} is half the angular aperture (or acceptance angle) of the objective lens. Considering that the pupil of the objective - which represents the maximum diameter of a parallel light beam which can enter the rear side of the objective, along the optical axis – has a radius Y of:

$$Y = (NA)f, \tag{6}$$

where f is the focal length of the objective lens. Eq. 5 can then be written as:

$$Y = fn \sin(\theta_{MAX}). \tag{7}$$

One can then use Eq. 7 to correlate the distance from the center of the pupil Y_{eff}, which coincides with the center of the BFP produced inside the objective, to the effective θ_{eff} light angle leaving the objective and hitting the sample below it:

$$\theta_{eff} = \sin^{-1}\left(\frac{Y_{eff}}{fn}\right). \tag{8}$$

The f of an objective lens can be calculated through analytical methods, but those require a deep knowledge of every component inside the objective, so a simple method was used to make this correlation. As it will be explained further in the thesis, the maximum displacement of the beam in the BFP has a 2 mm size. Considering this as Y, and using $\theta_{MAX} = 44.4º$ for an objective with an NA of 0.7, one can then assume that $f = 2.9\ mm$, and a relation between Y_{eff} and θ_{eff} can be calculated.

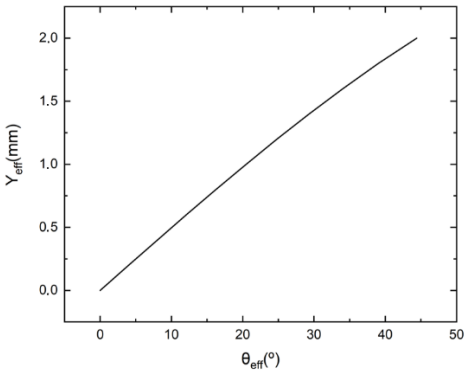

Figure 8 - Relation between the displacement of the beam in the BFP to the illumination angle of the sample.

An almost linear relation can be seen between the displacement of the beam in the BFP - correlated to the displacement of Lens 1 in the setup– and the angle of the light thereby hitting the sample below the objective (Figure 8).

2.3.2 Building and alignment of the Fourier microscopy setup

To facilitate the placing of all the components, they are mounted in a breadboard table with self-levelling active supports, which offers an ergonomic workstation optimized for most microscopy or photonics applications.

Since the most important thing in any optical setup is the correct alignment of the light path within all the components, a reference height was defined using a pinhole screwed on a post that is mounted in a post holder. This master pinhole is important as it will be used to align all the components of the setup.

The building and alignment of the setup were started on a table below the one where the setup sits - since this was the best solution found to correctly place Lens 2.[1] It is important to make sure that this beam is spatially aligned throughout its path, and for that, the master pinhole is extensively used in different positions of the path to ensure that. This procedure will systematically be used to align any component of the setup.

To align Lens 2 the objective was put into a vertical holder between Mirror 5 and Mirror 3. The light path in the bottom table was initiated using a 405 nm diode laser. The collimated light beam enters the pupil of the objective and is focused into its back focal plane; it then diverges until hitting Lens 2. If this lens is at its correct focal distance from the BFP, then the light coming out of it should be collimated, which can be easily checked by measuring the beam size over distance (Figure 9). The same procedure was done to align Lens 1. Mirror 5 and 3, and BS 1 (beam splitter with a 50/50 ratio) were aligned beforehand with the use of the master pinhole.

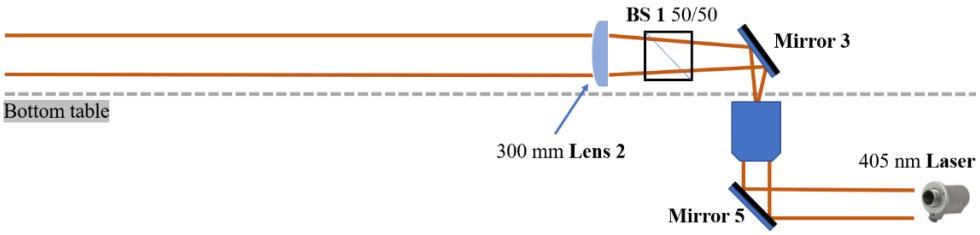

Figure 9 - Schematic of the procedure to align Lens 2.

After this, Lens 2 and the objective are removed from their respective mounts, and the CCD (2) camera is placed in the optical path after Lens 5. The laser beam hits this lens in a collimated way, and then it gets

[1] Photos of the setup can be found in the Appendix section (Appendix 1 and Appendix 2).

focused at one focal distance in the CCD camera. The CCD camera is connected to a computer, where the user can see in real-time the shape of the laser beam – when this shape has the smallest possible size, one can confirm the camera is at the right focal distance from Lens 5 (this takes into consideration the assumption that the incident beam is perfectly collimated), as seen in Figure 10.

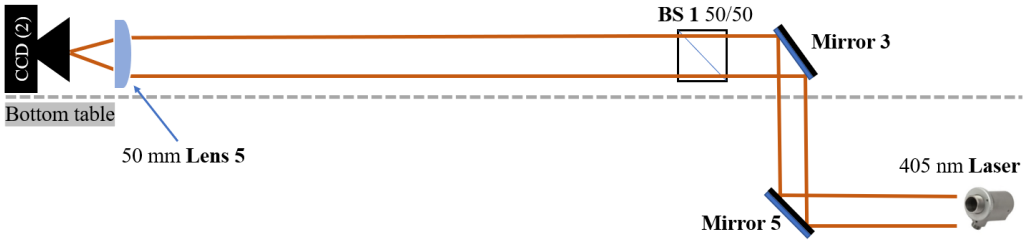

Figure 10 - Schematic of the procedure to align Lens 5.

Lens 2 is then added again to its mount, and Lens 3 is added between Lens 2 and Lens 5. What happens is that the collimated beam of the laser will hit Lens 2 and get focused at 1 f from this lens, and then diverge until hitting Lens 3. If Lens 3 is at 1 f from the intermediate focal point from the lenses, then the beam coming out of it will be collimated. The collimated beam will hit Lens 5, that will focus it on the CCD camera, whereas the smallest point should be seen, guaranteeing that Lens 3 is in the right position (Figure 11).

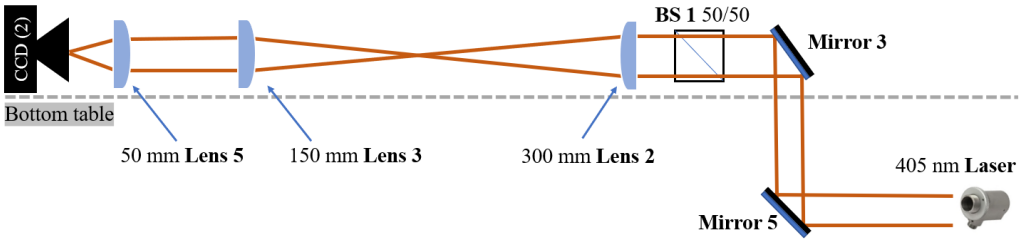

Figure 11 - Schematic of the procedure to align Lens 3.

Having the position of Lens 3 fixed, one can then remove Lens 2 and Lens 5 from their respective mounters. The collimated beam will hit Lens 3 and be focused at 1 f from this lens, where the CCD camera is moved to, in order to achieve the smallest beam spot captured by this camera, guaranteeing that it is at the focal distance of this lens. The beam spot presented by the CCD (2) camera for the alignment of the lenses described above can be found in Appendix 3.

After the components described above are aligned, the bottom path is no longer required, and Mirror 5 and the 405 nm laser can be removed. To align the two light paths on the top table, two pinholes are put in the vertical arm where the objective usually sits. For the Fianium path (depicted in blue in Figure 6), Mirror 1 and Mirror 2 are placed making sure that the light makes a 90º shift when hitting each one. These mirrors have mechanical screws embedded in their mounts, which are used to ensure that the light passes exactly through the middle of the pinholes placed in the vertical arm. By doing this, one can ensure that the light path will hit the middle of the BFP of the objective when the latter is put into place. The same procedure is valid for the white lamp path, using Mirror 4 and Flip Mirror 1. If this is done correctly, the beam passing through Lens 1 should be in the same optical path as the one reflected by it, which can be checked with a piece of paper at different positions of the path.

When the collimated Fianium beam hits Lens 1, it will be focused at its focal distance in the BFP of the objective, which then hits the cell with a collimated beam and gets reflected back into the objective. The objective will diverge the beam until it reaches Lens 2, where it will get collimated again. According to the optical principles described in the Introduction section, since Lens 2 is at one focal distance from the Fourier

plane (BFP), it will collimate the light coming from this plane and it will produce a real plane image at one focal distance in the other direction, thus its representation with red dashed lines on Figure 6. By being placed at 1 f from this intermediate plane, Lens 3 will image the Fourier plane on CCD (2). To create a copy of the intermediate imaging plane on CCD (1), the most straightforward way is having a lens at 2 times its focal distance from the real image, whereas an inverse replication from this plane will appear at the same distance in the other side of the lens. To be able to see the real image of the sample, the BS 2 was put into place, as well as an extra CCD 1 camera with Lens 4 attached.

When working with the setup one must always use safety eyeglasses. The measurements should always be done in the dark so that the ambient light does not impact the results.

3

RESULTS AND DISCUSSION

3.1 Setup calibration

Due to the complexity and amount of optical components required, the setup needed a large space. Because of this, the path that the light travels, becomes considerably long (> 1 meter), and this might have implications on the results, since a small misalignment of the components on one corner of the setup will become a big misalignment at the other corner of the setup. To minimize the chances of this from happening, multiple steps were conducted to calibrate and characterize the Fourier microscopy setup before starting the measurements.

3.1.1 Grating calibration

To calibrate the pixels of the CCD camera to the Fourier plane, a commercial 600 nm/groove grating was used. The grating was placed in the sample holder of the Fourier Setup which was manually moved into the right focal position of the objective using a 3D stage, and the diffraction orders of the grating can be seen in the Fourier plane, as presented by Figure 12. This in an implication of the Diffraction Grating equation (Eq. 9) that is based on the Huygens-Fresnel principle which states that when light goes through an aperture, every point of the light wave within the aperture can be viewed as creating a circular wave that propagates outward from the aperture [53]. The same can be replicated with a grating whereas when a parallel beam of light is directed normally at the diffraction grating, light is diffracted by the grating in certain directions only, i.e., the diffracted light waves from adjacent slits reinforce each other in certain directions only (including the incident light direction) and cancel out in all other directions – those are the so-called diffraction orders.

$$n_d \lambda = d \sin(\theta). \tag{9}$$

In this formula d is the spacing between grooves, n_d the order of diffraction, λ the light wavelength, and θ the correspondent angle.

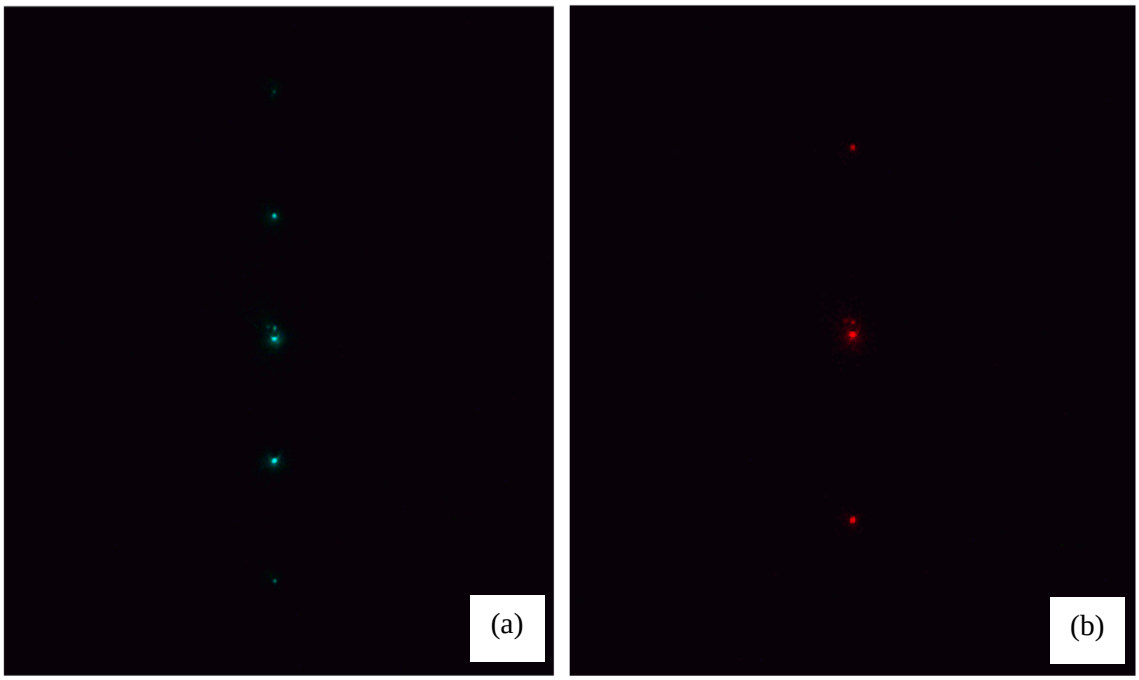

Figure 12 - Diffraction orders produced by a 600 nm/groove grating - as seen on the Fourier camera - for an incident light wavelength of (a) λ = 500 nm, and for (b) λ = 650 nm.

Being able to see a clear image of the diffraction orders on the CCD camera for different wavelengths is a good indication that the setup is properly aligned, whereas moving any component slightly out of its place will produce a distortion in the image. The slight brightness around the diffraction orders might be representative of a very small misalignment of any component adding to some saturation produced by the camera. One can then change the wavelengths of the Fianium laser and use Eq. 9 to calculate how many diffraction orders should appear in the Fourier image. For instance, when using an objective with a NA of 0.7, which corresponds to a maximum angle of collection/emission of 44.4º, and using an incident light with λ = 500 nm, 2 diffraction orders should be produced (Figure 12 (a)). For λ = 650 nm, only one diffraction order should appear (Figure 12 (b)). If the diffraction orders seen on the Fourier plane did not correspond to these calculations, there could be something wrong in the alignment, or the objective could be damaged (assuming that the grating is in good condition).

3.1.2 Mapping the Fourier space

It is now known that the objective has a maximum angle of collection/emission of 44.4º, thus this angle corresponds to the maximum displacement of the beam on the Fourier image (allowed by moving Lens 1) in relation to the center of the image. This distance corresponds to a 2 mm displacement of Lens 1 in all directions (Figure 13). If Lens 1 is moved more than 2 mm in one direction, the beam will disappear from the BFP as it hits the critical angle allowed by the objective.

Figure 13 - Beam displacement on the Fourier image in different directions allowed by the movement of Lens 1. The circle in blue denotes the BFP limits corresponding to a 2 mm displacement of the lens (when using a 0.7 NA objective).

3.1.3 Beam displacement on the samples

Since the basic principle of the Fourier microscopy setup is to displace the beam on the BFP of the objective, which will then hit the cell at a certain angle, the displacement of this beam at different angles needs to be studied. If this displacement is too big, the beam might not hit the cell fully or partially.

To understand the beam displacement over all angles, a 1951 USAF resolution test chart was used (Figure 14 (a)). The standard pattern of the chart consists of 9 groups, with each group consisting of 6 elements. Each element consists of three bars aligned horizontally and three vertically. The smallest set of bars of this target measures a total of 11 µm (2.19 µm each bar and 2.19 µm each spacing between bars). When placed on the sample holder, an image of this target can be seen on the CCD camera (real space), and a direct pixel measurement can be made on top of it. As depicted on Figure 14 (b), the set of bars measuring 11 µm corresponds to 94 pixels on the CCD camera. This measurement was done using the white light path as it would be harder to see the target clearly with the Fianium laser using single wavelengths.

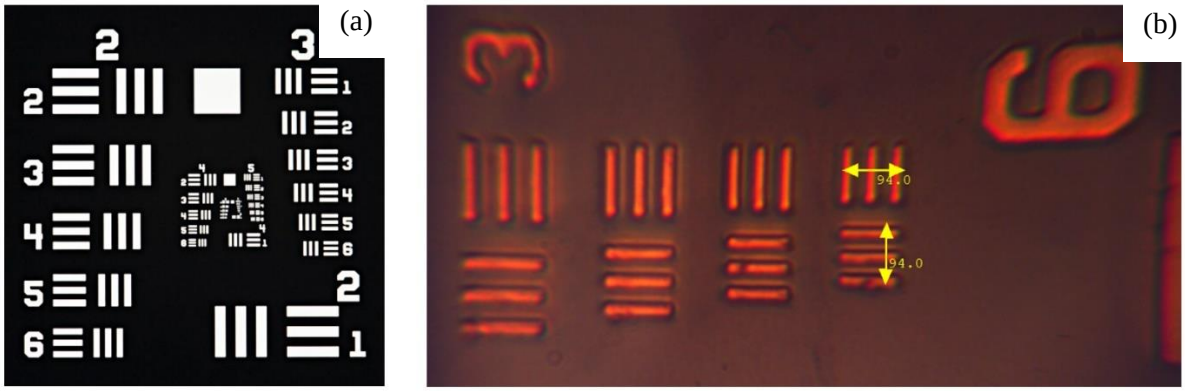

Figure 14 – (a) the 1951 USAF resolution test chart used for calibration; (b) the real image of this target given by the CCD camera.

To measure the full displacement of the beam on the cell, the Fianium was used at an arbitrary wavelength of 600 nm. Lens 1 was then displaced by 2 mm to one side - covering the whole range of angles defined by the NA of the objective. By measuring the pixels directly on the CCD camera (real space), it is then possible to conclude that the beam has a maximum displacement of 1432 pixels which corresponds to 168 microns, which is an extremely small displacement compared to the solar cell sizes (Table 1), thus making sure that the light beam will always hit the cells at every angle considered.

To check for any colour aberrations that the setup could have, the beam displacement in the real space was studied for different incident angles, using the CCD (1) camera. In Figure 15 (a), one can see that there is no major difference in the displacement of the beam for different wavelengths. While performing these measurements it became clear that the beam waist enlarges over different angles. This change in size is presented in Figure 15 (b). Since the beam has a circular waist, this measurement was done in one direction only (horizontal), although for higher angles, the beam gets elongated and its size in the vertical direction should be

considered for future improvements on the calibration. It is possible to see that not only the beam waist increases with angle, but it also increases with longer wavelengths. A possible explanation is given on the next sub-section.

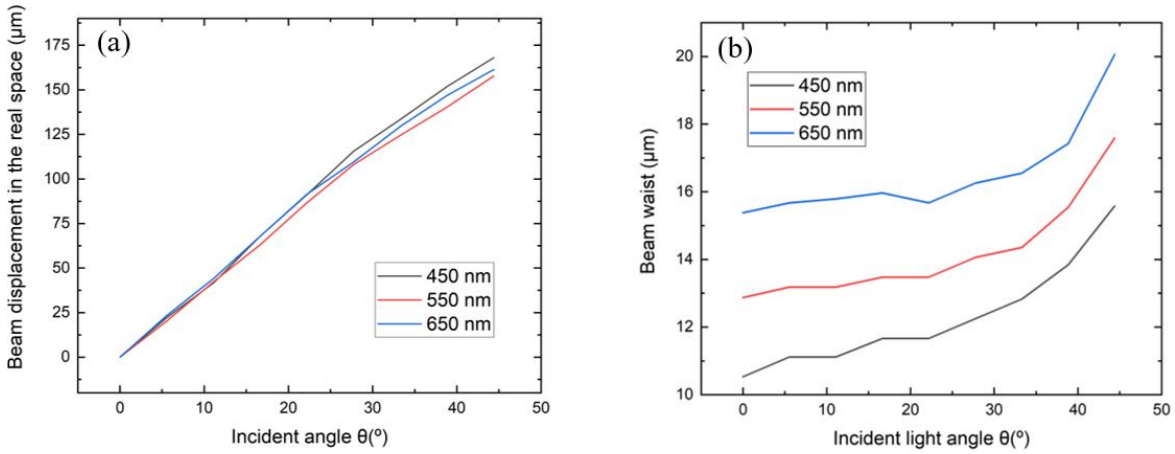

Figure 15 – (a) Beam displacement seen in the real space for different angles of incidence and wavelengths; (b) changes on the beam waist seen on the real space for different angles and wavelengths.

3.1.4 Laser intensity

As was already described, the Fianium laser allows for a multitude of light wavelengths, ranging from 300 to 1100 nm. Although it is also recommended by the manufacturer to use wavelengths longer than 450 nm for applications where a high accuracy is needed. Since the wavelengths corresponding to the peaks and dips of the simulated absorption plots of the solar cells are all above this value (Figure 20), this range had no impact on the experimental results of this thesis. To better analyze and describe the laser source of the Fourier Setup, Table 2 is presented with a list of all the light wavelengths used for the experimental results as well as their power, recorded with a power meter. The power of the laser does not represent the intensity of light - generated by the sun – as in a real-life application, although it serves as a reference for measurements.

The laser power increases for longer wavelengths. This could explain why the beam waist also gets larger for longer wavelengths.

Wavelength (nm)	450	500	550	596	600	614	617	628	650
Power (mW)	0.263	0.738	1.241	1.451	1.453	1.541	1.583	1.592	1.663

Table 2 - Power measurements of the Fianium laser for different wavelengths.

3.1.5 Correcting the focus of the laser

To properly use the setup, the focus of the laser plays a big part in the overall results. For instance, if this focus is slightly off in one measurement, the beam spot in the Fourier camera will have a larger size than what is supposed to, diminishing the accuracy of the results. A proper way to know that the objective is correctly placed at its focal distance from the target is to see the real space image in the CCD camera. First, the solar cells are put into place in the EQE box, which is then mounted to 3D stage holder that has millimetric screws that enables the user to precisely move it in X, Y, and Z directions. The white lamp is used because the real image produced by it is clearer than by only using a single wavelength with the Fianium laser. Lens 1 is removed from its holder, ensuring that the light hitting the cell is focused. This lens is placed back after a correct focus is achieved. Then, the EQE holder is put into a place where the light hits the cell to be measured;

this can easily be done by eye. The holder is then slowly moved towards the objective (making sure it does not touch it, to not cause any damage), while watching the real space image provided by the CCD camera. At a considerable distance from the objective (i.e., > 5mm), the real space camera only shows a distorted image that represents the non-focused light reflected by the EQE box. Moving the sample closer to the objective, one can then see a more focused light and even some shapes and forms – this means that the focal distance from the objective to the glass of the EQE box was achieved, and some artifacts, mainly dust or scratches, are visible at this point as shown in Figure 16.

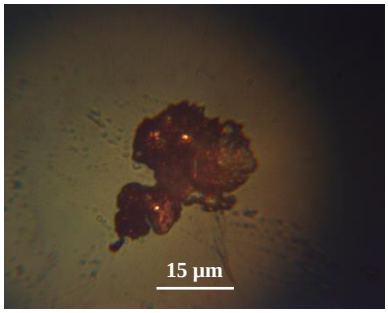

Figure 16 - Dust particles seen on top of the glass of the EQE box.

This is the first focal point (on the back side of the glass substrate). The samples to be measured are below this glass, so the sample holder should be moved further close to the objective until another focal point is achieved. This procedure should be checked every time before a measurement is done in order to assure that the focus is indeed on the sample. If the focus is correctly adjusted, the border of the cell with the contact surrounding it, as well as the borders of the contact with the empty surrounding media of the EQE box can clearly be seen, as presented by Figure 17 (a) and (b).

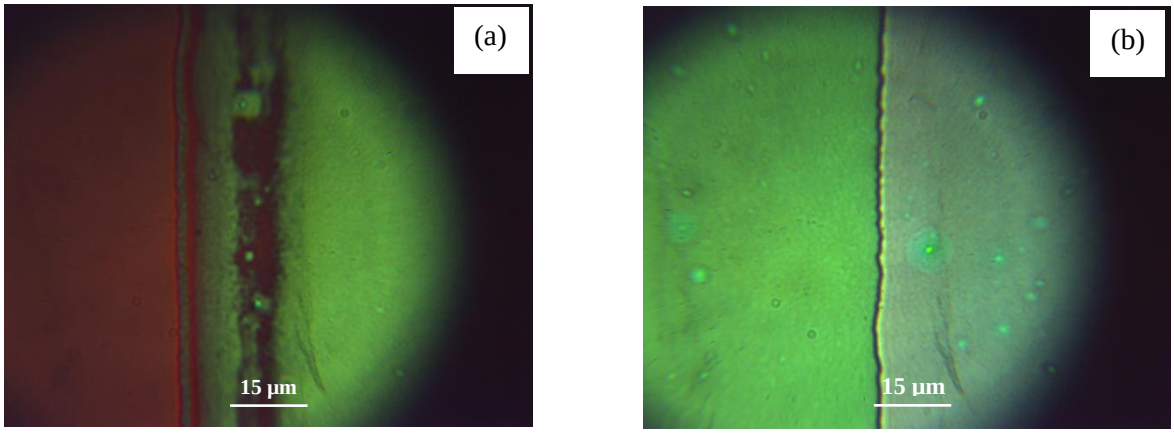

Figure 17 - Real space image of the (a) border of the cell contact (light green) with the empty surrounding media (red); (b) border between the cell contact (light green) and the P355 cell (sage green).

3.1.6 Reference measurement

The Fourier setup was designed to be able to measure the J_{SC} produced by a sample for different angles of incidence. It makes use of a homemade LabVIEW program which maps the current obtained with the multimeter attached to the EQE box for every X and Y position that Lens 1 is moved to. To run the program, the starting and ending coordinates of the measurement need to be set, the multimeter needs to be connected to the coaxial pin of the solar cell, and the stepping of the movement in X and Y needs to be defined. The program then runs automatically, displacing Lens 1 in X and Y, thus shifting the angle that the light beam makes with the normal to the sample. The measurements were done for each individual cell, setting the wavelengths of illumination, as well as an arbitrarily beam power, on the computer program that controls the Fianium laser,

while always making sure that the sample is placed in the focal distance of the objective. To ensure that the measurement covers all the angles allowed by the NA of the objective, those measurements were done by displacing Lens 1 5 mm to each side, with the starting position at X = 0 and Y = 0. The position X = 2.5 and Y = 2.5 will then be the central position of the BFP corresponding to the laser beam hitting the cell at 0º. As an example, since the BFP had a measure of 2 mm, the position Y = 2.5 and X = 4.5 will correspond to the edge of the BFP which indicates that the light beam is hitting the cell at θ = 44.4º. Since the displacement of the Lens can be in X and Y, the angle that the beam makes with the sample will also have two directions that will be denoted as θ and φ respectively, in similar correlation to the spherical coordinate system.

A polarizer can also be added to the setup between Mirror 1 and Mirror 2 of Figure 6. To do a reference measurement on the setup, a polarizer at 0º was used, which can also be called an x-polarizer or horizontal polarizer. One can then denote a TE or TM excitation along the axis of the measured color plot. An incident plane wave has a wave vector component parallel (k_y) and perpendicular (k_z) to the substrate. The TE mode corresponds to when the lattice adds momentum along the parallel component of the incident wave vector, while for the TM mode the lattice momentum vector is perpendicular to the k_y component of the incident wave. Following this assumption, if the incident beam is moved in the X direction it will excite TM mode along this direction, and if it is moved in the Y direction it will excite the TE mode [54].

For the reference measurement, the current of a commercial silicon photodiode was measured for different incidence angles (Figure 18). This was done using an arbitrary wavelength of 596 nm.

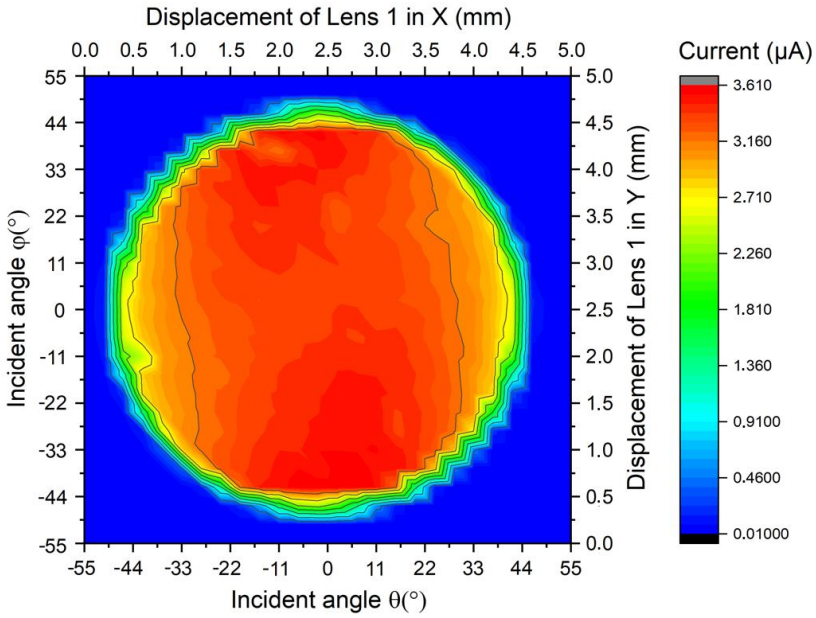

Figure 18 - Colour map of the current produced by a silicon photodiode by displacing Lens 1.

Since the displacement of Lens 1 to each side in X and Y (considering X = Y = 2.5 the central position) represent the same angles, a 2-fold rotational symmetry can be seen on these color plots. It is also possible to see that the diameter of the circular color maps is slightly bigger than the expected 4 mm (corresponding to the BFP size of the objective). An explanation for this might be that for an incident light angle higher than 44.4º (e.g.: θ = 45º), there is still a residual intensity of the laser beam that still enters the objective, and this is due to the fact that the focused beam on the BFP is not a single point, as it can be seen on Figure 13.

The size of the beam on the BFP can explain why there is a disparity in current at larger angles (i.e.: θ > 40º, or φ > 40º), as it starts hitting the edge of the BFP of the objective (as seen on Figure 13) which can create some extra reflections inside the objective that hit the cell at different angles; thus those specific values of current should not be considered as accurate.

Using a single line of current values from Figure 18, the J_{SC} behavior of this silicon device for different angles of incidence is plotted on Figure 19 (a). Those values consider the relation between the current (I) provided by the multimeter and the area of the incident beam (A) at different incident angles (Figure 15 (b)), whereas $J_{SC} = I/A$.

Only an angular range from 0º to 40º is presented, since the values obtained for higher angles do not present the real behavior, as explained above. For comparison, a similar code of the TMM used in the simulation of the planar solar cell was then modified to simulate the J_{SC} plot of the same silicon device, considering the same angles (Figure 19 (b)). This was done for both TE and TM modes, and unpolarized light. In the simulated plot, it is possible to see an increase in current when the TM mode is excited, from 0º to 44.4º; whereas on the other hand, the TE mode decreases in current for the angular range considered.

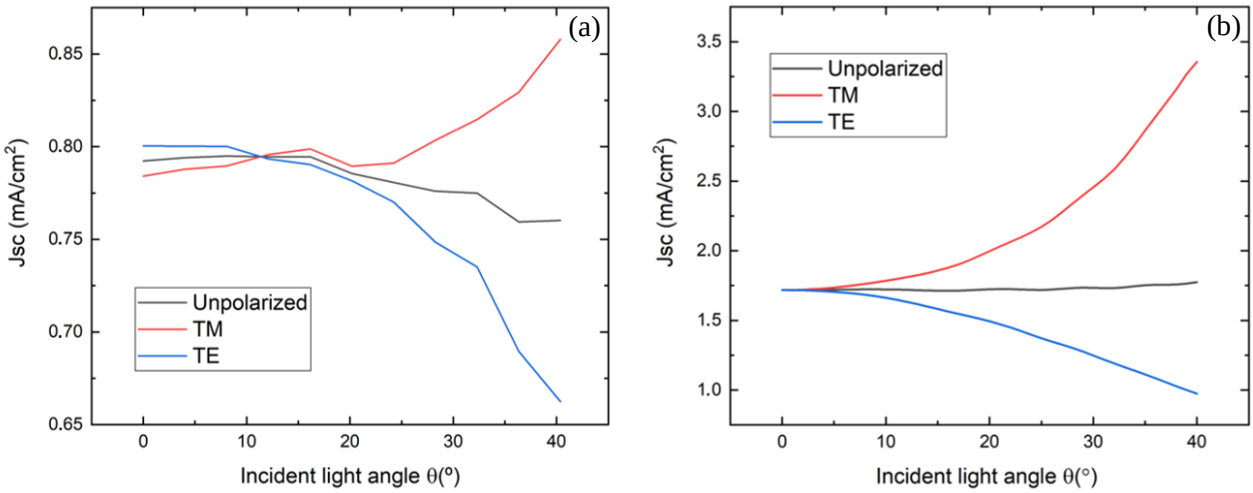

Figure 19 - (a) J_{SC} measurements taken from the colour map, considering φ = 0, and θ = 0º to θ = 40º for the TE measurement; and θ = 0, and φ = 0º to φ = 40º for the TM measurement. The J_{SC} was calculated through the formula $J_{SC} = I/A$, considering the area of the beam waist for different angles; (b) simulated J_{SC} for the same device, using a TMM.

Comparing the simulated results with the experimental data, one can consider that the overall behavior of the angular dispersion is accurate, even though some noise is expected due to any small misalignment or dust present in any component of the setup. The difference in values between simulation and experimental results can be expected, as the simulations consider a perfect device. Since the area of the beam increases over different angles, this means that the J_{SC} will decrease faster than the simulated device, whereas a constant area was considered for all angles. Taking those things into consideration, this plot gives a fair degree of trust to the results given by the Fourier setup, indicating that it has a good alignment. It came as a late conclusion during this thesis that the unpolarized J_{SC} in Fig 19 (b) was not calculated correctly and should have a small increase for higher angles, although the results could not be replicated due to the loss of the original code of the simulation. Although, the TE and TM modes were well simulated, and those provide a fair degree of trust to the setup.

3.2 Simulations for the solar cells

Before making use of the setup to analyze the J_{SC} on the solar cells, computer simulations were made. From these simulations one can better understand what the behavior of the real solar cells under different angles of illumination should be. The first simulations shown in the section were done using Lumerical, although due to technical limitations, COMSOL was later used. Additional simulations using MATLAB are also shown.

3.2.1 Lumerical simulations

To model the interaction of electromagnetic waves with nanostructures, the FDTD method can be used. For this numerical method, the space is divided into a grid, and a pulse (with the desired wavelengths) of electromagnetic radiation is introduced. The electric fields can then be recorded, and the transmission and reflection characteristics, as well as the near fields can be calculated.

As described earlier, Lumerical was firstly used to simulate the solar cells with metallic nanoparticles. The simulations used PML boundary conditions. These boundary conditions make use of a single element cell of a periodic structure that is illuminated with a plane wave source propagating at a certain input angle. Regarding the simulations, the absorbed power per unit volume can be calculated from the simulated electric field distribution, which is calculated with the formula:

$$P_{abs}(x,y,z,\omega) = \frac{1}{2}\varepsilon_0\omega|E(x,y,z,\omega)|^2\varepsilon''(\omega), \quad (10)$$

where $E(x,y,z,\omega)$ is the electric field at coordinates x,y,z and at the angular frequency ω, ε'' is the imaginary component of the permittivity of the material at the same coordinates and ε_0 is the vacuum permittivity. The absorptance of the organic blend in the solar cell can be calculated as:

$$A(\omega) = \frac{1}{P_{source}}\iiint_V P_{abs}(x,y,z,\omega)dxdydz, \quad (11)$$

where P_{source} is the power of the incident wave and V is the volume occupied by the blend (Figure 5). By assuming an internal conversion efficiency of the organic blend of 100%, i.e, the number of generated electron-hole pairs is equal to the number of absorbed photons, the J_{SC} of the solar cell can be determined as

$$J_{SC} = \frac{e}{\hbar S}\int_{\omega_1}^{\omega_2}\frac{A(\omega)S_{AM1.5}}{\omega}d\omega, \quad (12)$$

where e is the electron charge, $\hbar$ is Planck's constant, S is the surface area of the device and the $S_{AM1.5}$ is the AM 1.5 solar spectrum of the organic blend. The J_{SC} value obtained may be assumed as the maximum current value that the solar cells will produce, considering ideal electrical behavior in the electron-hole generation process. The integral limits are defined by the absorption spectrum of the organic blend corresponding to wavelengths in the range of 300 to 1100 nm.

Figure 20 shows the normalized absorption spectra of the blend of the four cells studied, for normal light incidence. It is possible to see that in these cells, the metallic nanoparticles deteriorated the blend absorption. The electric fields shown in the sub-section 3.2.3 aim to better understand the peaks and dips in these absorption spectra.

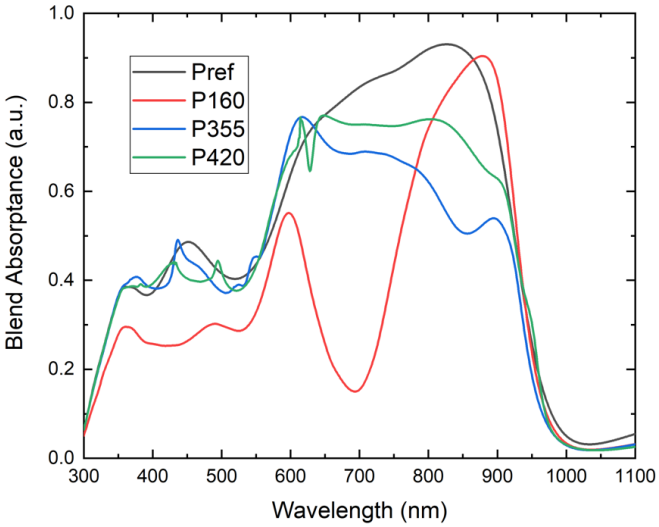

Figure 20 - Blend absorptance spectra for the four solar cells.

To understand the effect of the angle of incidence, simulations were firstly done for the P160 solar cell, where the J_{SC} was calculated for different angles using a TM (transverse magnetic mode) polarized light source, for 300 to 1100 nm – which covers the spectrum of visible light and near infra-red. From these simulations, an increase in the J_{SC} of the device is noticeable for θ = 25º and θ = 30º, having then a strong decrease for higher angles, as seen in Figure 21. The abrupt decrease for higher angles is unusual comparing to lower angles and a further study is needed to verify these results.

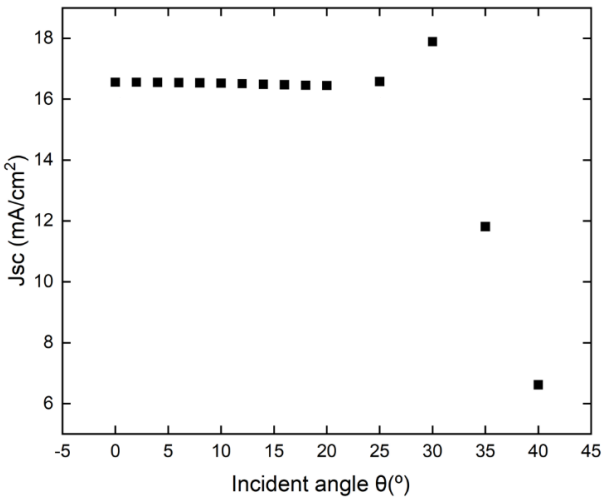

Figure 21 - J_{SC} of the P160 solar cell for different angles of incidence.

Since the J_{SC} is correlated with the absorption of the light by the device, a study of the absorption of the blend as a function of wavelength for different angles was conducted, as shown in Figure 22 (a). In this figure, for certain wavelengths (e.g., 695 nm) there is a small increase of the absorption of the blend, whereas for other wavelengths (e.g., 595 nm) there is a decrease. For longer wavelengths, a slight blue-shift (a spectral shift towards shorter wavelengths) in the absorption curve is also noticeable. On the other hand, a slight redshift is noticeable at wavelengths around 1000 nm, although the absorption of the blend is low at these wavelengths.

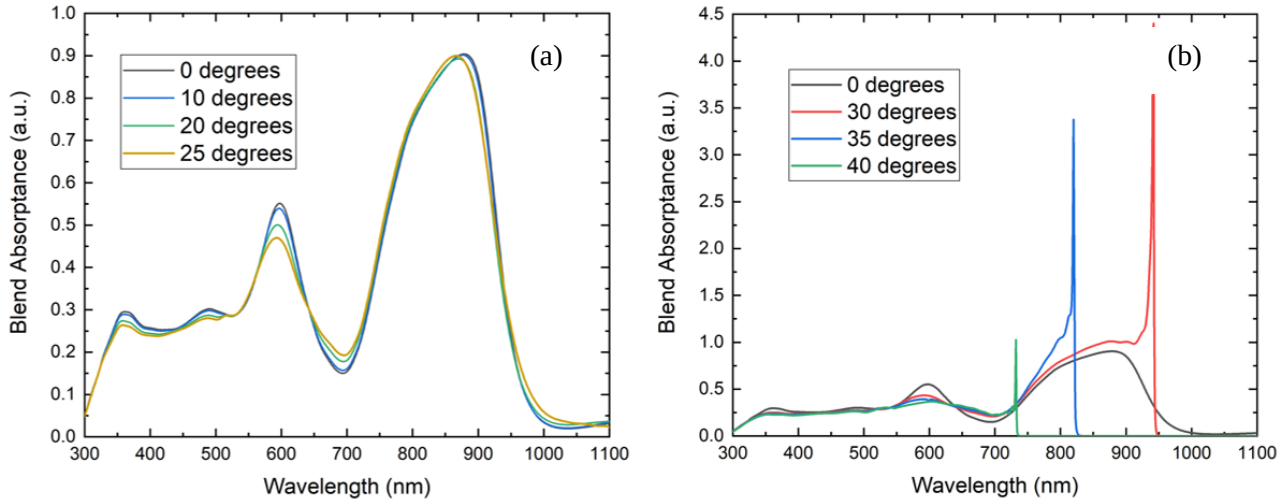

Figure 22 - Blend absorptance simulations for a 300 - 1100 nm wavelengths range for (a) 0, 10, 20 and 25 degrees on of Incident light, and for (b) 0, 30, 35 and 40 degrees.

Even though Lumerical is a common option to simulate plasmonic devices, after running multiple simulations it became clear that something was not working properly. This observation came after seeing the plots of the absorption spectrum for incident angles larger than θ = 25º for the P160 cell, as shown in Figure 22 (b). Even though for angles equal and lower than 25º the absorption plot seems to have a normal behavior, this clearly does not happen when doing the simulation for larger angles. In those plots, a strong peak in the absorption of the blend is observed at longer wavelength, i.e., longer than 730 nm, and then, at a certain wavelength, the absorption decreases abruptly to zero.

To further understand this issue and try to solve it, a reflectance monitor was added to every simulation, to see if those strange results also happened in the reflection produced by the cell. Different parameters were also changed in Lumerical hoping to optimize the simulation and thus have better accuracy: the simulation time, the auto shut-off limit, the mesh accuracy, and the number of layers associated with the boundary conditions. The absorption spectrum remained the same, while the reflectance observed in the new simulations resulted in Figure 23.

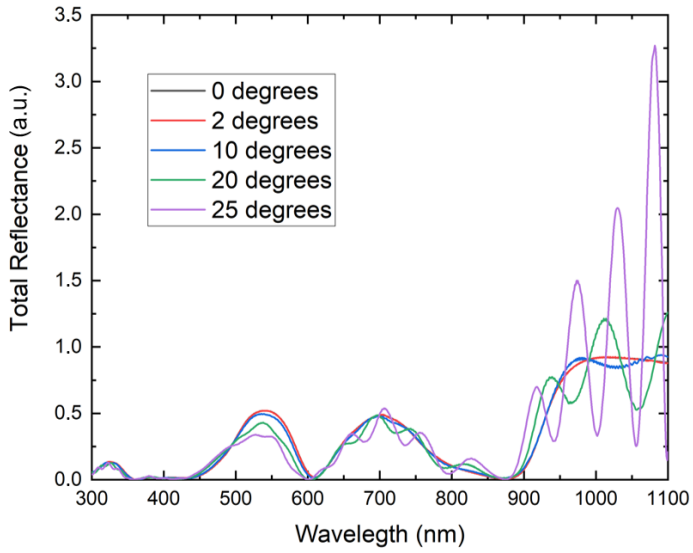

Figure 23 - Total reflectance produced by the cell for an incident plane wave at different angles.

The reflectance of the full device confirms that the simulation was not trustworthy, as it presents a very unstable behavior over all the wavelengths studied, and so, the first assumption that the J_{SC} was higher at

certain angles could not be confirmed. This issue could then be related to the fact that Lumerical works at a constant in-plane wave vector ($k_{in-plane}$) and not at a constant angle θ. This wavevector represents the direction of propagation of a wave. For instance, for a simulation running from 400 nm to 1000 nm wavelengths, with an incident plane wave of θ = 60º, Lumerical will use the central wavelength, i.e.: 700 nm, to first calculate the total wavevector (k_{total}) of the incoming light, using the formula:

$$k_{total} = \frac{2\pi}{\lambda} = 8.97\ \mu m^{-1} \tag{13}$$

It will then calculate the in-plane component of this wave vector by multiplying it with $\sin(\theta)$

$$k_{in-plane} = k_{total} \cdot \sin(\theta) = 7.77\ \mu m^{-1} \tag{14}$$

Lumerical will use this $k_{in-plane}$ for all wavelengths considered on the simulation – which means that for each wavelength, the incident light angle θ will be different. This becomes a problem for certain wavelengths. Considering λ = 900 nm, k_{total} has a value of 6.98 μm^{-1}; then, using the formula described above (Eq. 14), the corresponding value of θ is calculated:

$$\sin(\theta) = \frac{k_{in-plane}}{k_{total}},\ \theta = \sin^{-1}\left(\frac{k_{in-plane}}{k_{total}}\right) = \frac{7.77}{6.98} \tag{15}$$

This calculation has no real solution, as the inverse function of sin needs to have a value inferior to 1; therefore, it does not correspond to a real simulation condition.

3.2.2 COMSOL simulations

The simulations were then done in COMSOL, which is a frequency domain method as opposed to Lumerical (a time-domain method). The absorption spectra for different wavelengths was only simulated for the P160 cell – shown in Figure 24 (a) - as this was a very time consuming type of simulation. The blend absorption for different angles of incidence was also calculated the three solar cells with nanoparticles (Figure 24 (b)).

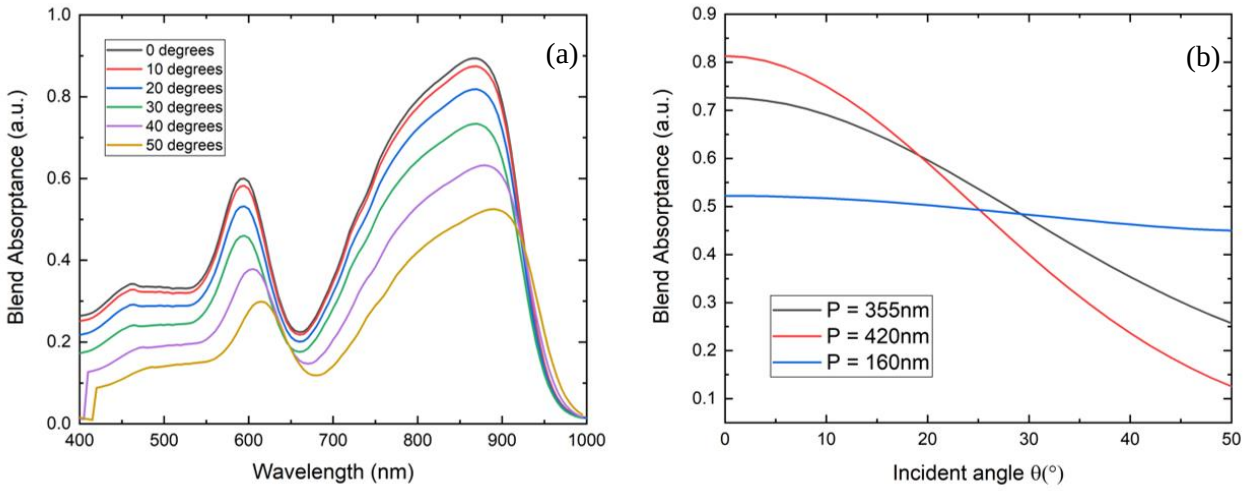

Figure 24 - (a) Blend absorption spectra for the P160 cell under different angles of incidence; (b) blend absorption spectra for different angles of incidence, for the plasmonic solar cells.

From those simulations one can see a decrease of the overall absorption of every cell, for every angle considered. Therefore, the J_{SC} will have this same behavior, according to Eq. 12. From Figure 24 (a), one can also denote that for the vast majority of wavelengths and angles, the introduction of the nanoparticles does not create a higher absorption in the cell. It comes as conclusion that any plasmonic effect created by the metallic particles on those cells does not have an angle dependency factor. The fact that the blend absorptance for the P160 cell in Figure 24 (b) has a small decrease over angle comes from the fact that this simulation was only done for a single wavelength, i.e.: 645 nm.

3.2.3 Electric Fields

Additional simulations for normal incidence were run on MATLAB using a homemade script, provided by PSN group member Ping Bai. In here, the spatial distribution of the normalized electric field intensity $|E|^2$ is calculated on the xz-plane, as a function of frequency f_λ , and x,y,z positions, through the formula:

$$E(z,f) = \iint |Ex(x,y,z,f)|^2 + |Ey(x,y,z,f)|^2 + |Ez(x,y,z,f)|^2 dxdy, \quad (16)$$

where $f_\lambda = \frac{1}{\lambda}$.

Those simulations can help understand the absorption spectra of the solar cells; thereby, the simulations were made for a few wavelengths representing peaks and dips on the absorption spectra. Only one wavelength for each cell is here presented, which will also be studied later in the Fourier setup: λ = 596 nm for P160; λ = 617 nm for P355; λ = 628 nm for P420.

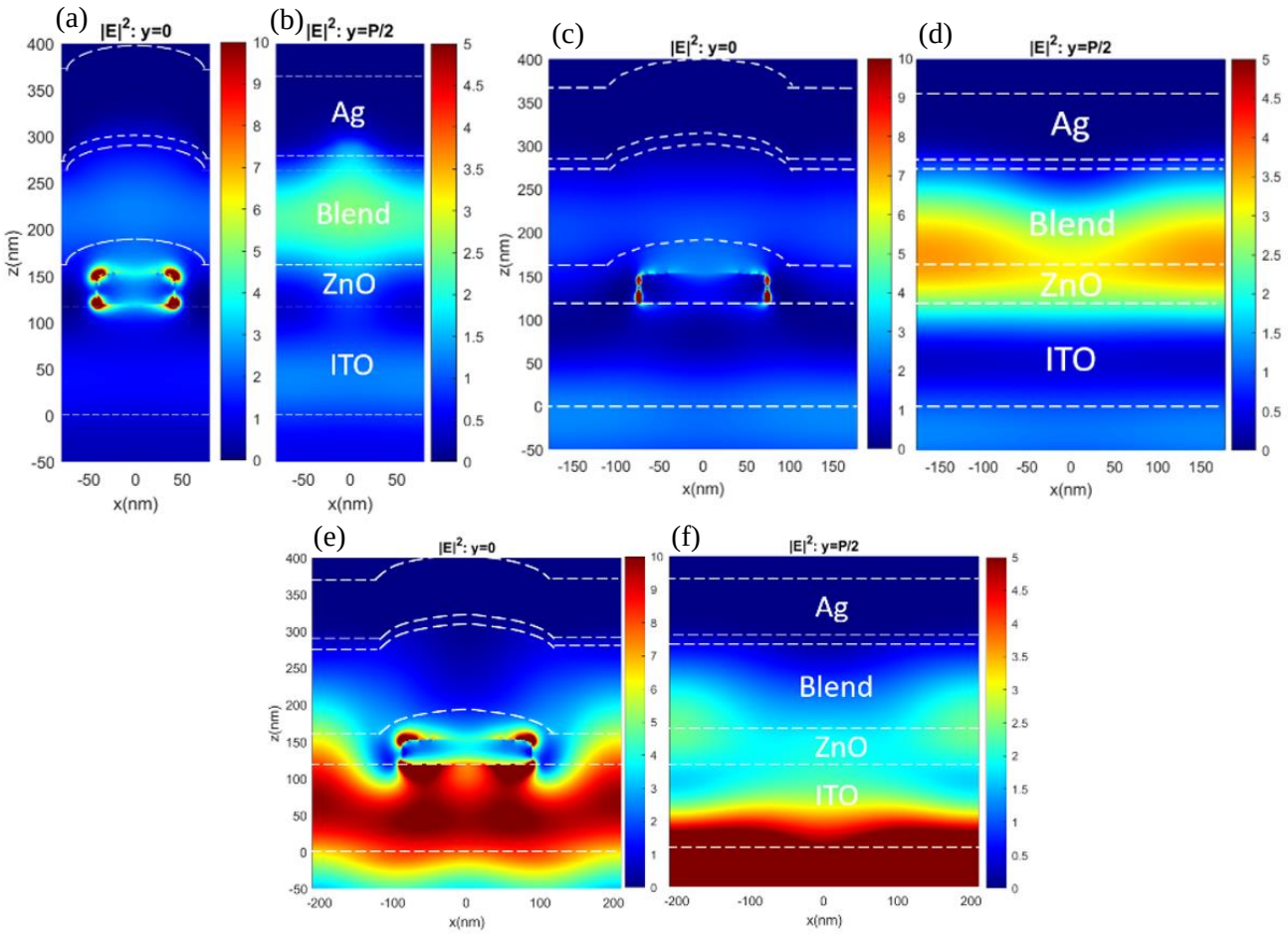

Figure 25 - Spatial distribution of the normalized electric field intensity for different cells and wavelengths: (a) and (b) correspond to the P160 at $\lambda = 596\ nm$, for $y = 0$ (field with the particle on the middle of the simulation) and for $y = P/2$ (field in-between particles) respectively; (c) and (d) correspond to the P355 at $\lambda = 617\ nm$, for $y = 0$ and for $y = P/2$; (e) and (f) correspond to the P420 at $\lambda = 628\ nm$, for $y = 0$ and for $y = P/2$.

At λ = 596 nm in P160 and λ = 617nm in P355 there is a peak in the absorption spectra (Figure 2020), and the electric fields confirm that there is a high absorption in the solar cells blend (Figure 25 (b) and (d)). This could be reminiscent of a waveguide resonance plasmonic effect, which usually happens in a layer sandwiched by two others with lower refractive index. This resonance happens when an incoming light wave is diffracted into multiple modes when it hits a periodic grating, and some of these modes can stay trapped in the surrounding of the grating thus creating a waveguide resonance. Since the first two examples happen in the absorber layer of the device, understanding if these plasmonic device have an incident light angle dependency is important. A similar thing happens at λ = 628 nm for P420 (Figure 25 (f)), although in this case the waveguide resonance happens below the grating, in the ITO layer, which causes a dip in absorption contrarily to the other two examples considered.

3.2.4 Characterization of the reference solar cell

Additional simulations were conducted using a Transfer Matrix Method (TMM) for the reference solar cell, while the COMSOL simulations were running for the solar cells with nanoparticles. The TMM describes the coherent passage of light through thin film layer stacks using 2 by 2 matrices. These are multipliable with each other and can then be used to calculate electric fields of light traveling inside the layered stack. The TMM is based on the Fresnel equations, although those could only explain the reflection of light from a single interface between two media and do not take into consideration the transmission and partial reflection created in a system with multiple interfaces, as it happens in thin film solar cells. This method takes into consideration the

refractive index, extinction coefficient, and thickness of every layer in the device, as well as the angle of incidence. Its calculation was done using the programming software MATLAB, and the complete code can be found in the Appendices section.

The color maps obtained, presented in Figure 26, represent the absorption spectrum for different wavelengths as a function of the incident light angle, and were done for both TE and TM light polarization. Since this is a planar device that does not have any type of nanostructures to interact with the light in the absorber layer, nor does it have any type of antireflection-coating, some reflection is expected. This event gets more intense at larger angles, where the reflection (as explained by Fresnel equation) of the device becomes larger than the absorbed light. This happens for both TE and TM in a similar way.

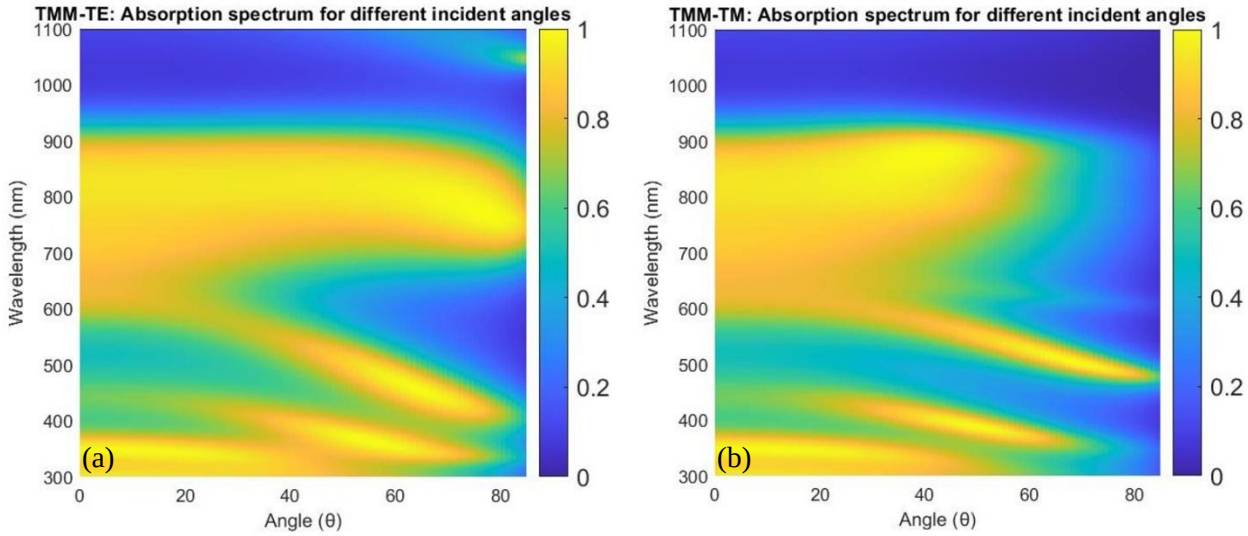

Figure 26 - TMM simulations for absorption of the planar solar cell, for (a) TE polarization and (b) TM polarization.

3.3 Solar cell measurements performed on the Fourier setup

The J_{SC} of the cells under different incident angles was studied using the Fourier setup. These measurements were done for each individual cell for the wavelengths that represent the peaks and dips of the absorption plots seen on Figure 20. Those peaks and dips are a clear indication of changes caused by the nanoparticles on the cell, thus they could have an increase in J_{SC} for certain angles, even though the absorption plots simulated with COMSOL do not indicate this. The colour plots thereby presented on Figure 27 follow the same methodology explained on sub-section 3.1.6, where a similar measurement was done for a silicon photodiode.

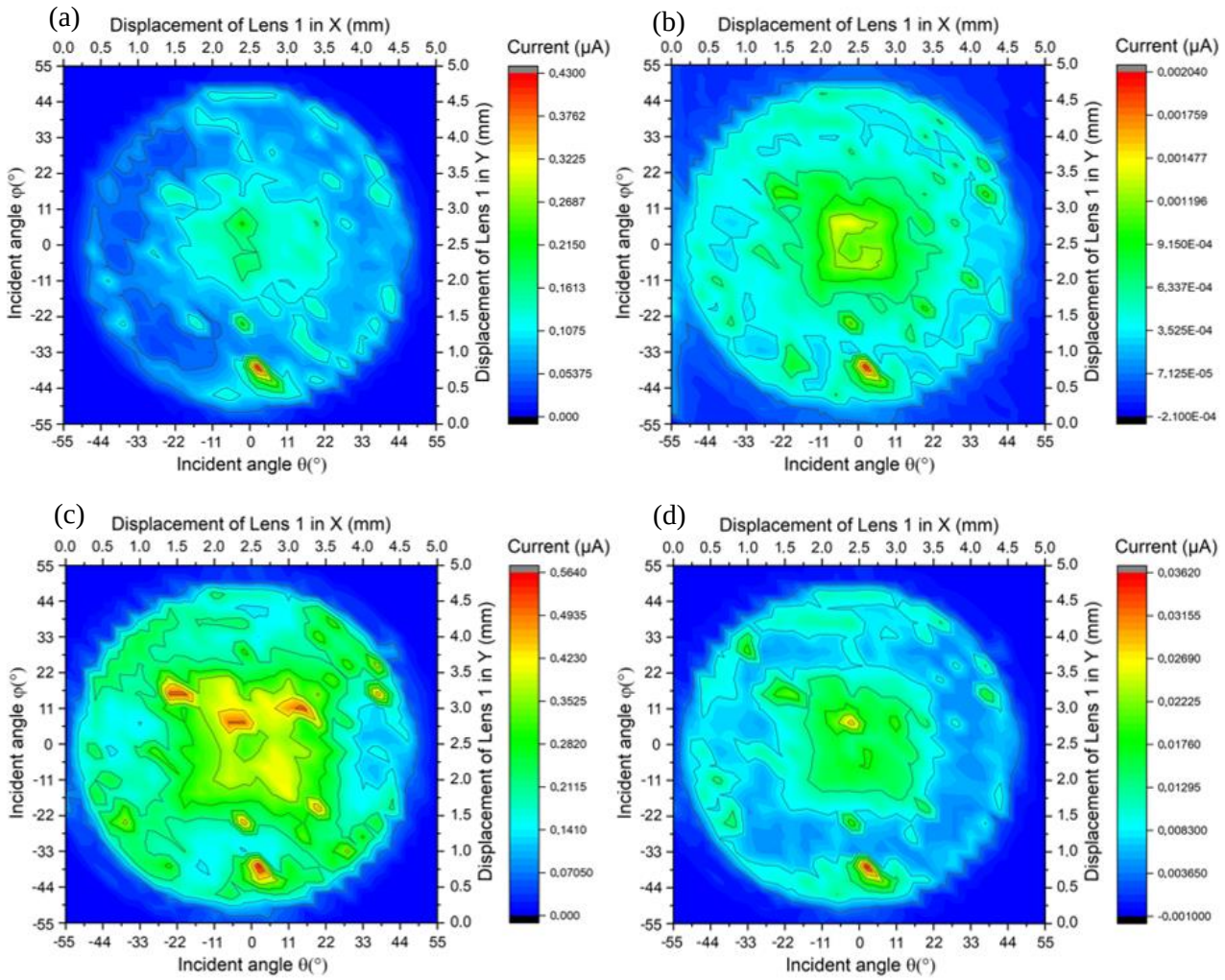

Figure 27 - Colour map of the current given by the samples in correlation to the displacement of Lens 1, presented for the four solar cells: (a) Pref, using λ =596 nm using a laser power of 0.5804 mW; (b) P160, using λ = 596 nm and 1.451 mW laser power; (c) P355, using λ = 617and 1.583 mW laser power; and (d) P420, using λ = 628 nm and 1.592 mW laser power.

A fourfold symmetry is expected to be seen on the colour plots, due to the symmetrical displacement of Lens 1 along X and Y axis. Although it is not exactly what is seen, the result does not differ much from that. Some noise is to be expected from small misalignments or even dust or scratches somewhere in the components of the optical path. The region of high current present in all measurements at X = 2.6 and Y = 0.7 could be an example of that possibility.

To analyze how the J_{SC} behaves for different angles of incidence and to compare it for all the samples, Figure 28 shows these values only for a straight line of φ = 0º, and θ = 0º to 44.4º.

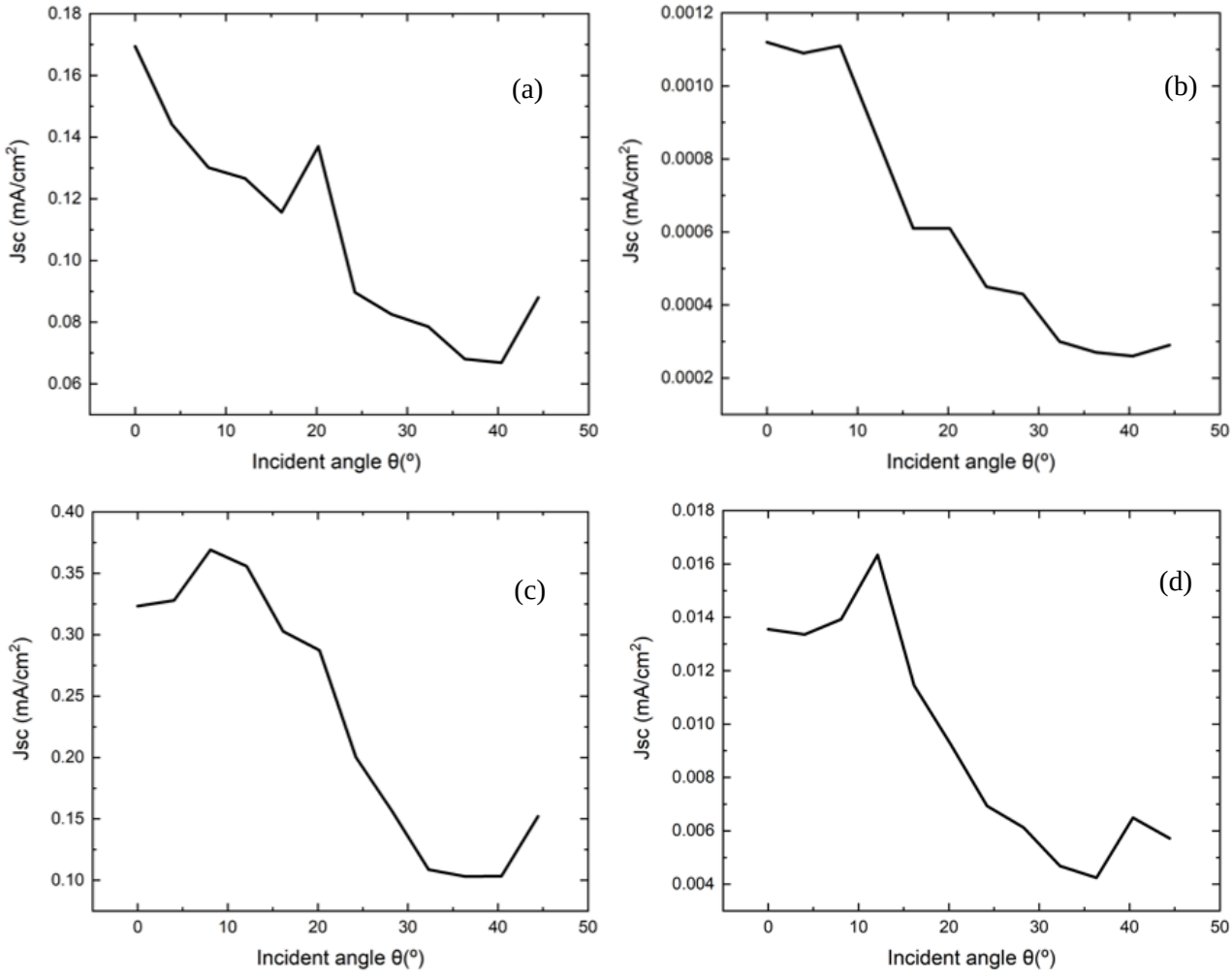

Figure 28 - J_{SC} measurements taken from a single straight line from the cells current colour map (φ = 0º, and θ = 0º to 44.4º), whereas: (a) Pref, using λ =596 nm using a laser power of 0.5804 mW; (b) P160, using λ = 596 nm and 1.451 mW laser power; (c) P355, using λ = 617 and 1.583 mW laser power; and (d) P420, using λ = 628 nm and 1.592 mW laser power.

Analyzing these measurements, one can see an overall decrease in the J_{SC} with angle of incidence, which matches with the COMSOL simulations (Figure 24 (b)).

In the J_{SC} plots obtained from the color plots (apart from the reference cell) a slight increase in the current values happens for small angles. This consistent behavior for different solar cells could indicate that something was not correctly working. A possible explanation is that the cell was being bleached by the laser prior to the measurement – since, for the alignment of the setup and starting of the computer program that controls Fianium, the laser is hitting the same position of the cell (at 0º) for some time. This bleaching could then decrease the properties of the cell in this starting position and then an increase in J_{SC} is seen, as the laser moves through the cell for higher angles. It could also happen that there are parasitic reflections from a scratch in any of the optical components of the setup entering the objecting, and thus hitting the cell, for certain angles. Apart from that, the increase in current at higher angles is due to the beam hitting the edge of the BFP as explained in sub-section 3.1.6.

The planar solar cell plays a major role when analyzing the results, since it is considered the reference cell (Figure 28 (a)). In this device, the overall J_{SC} decreases as the angle of incidence increases, as it is expected according to the Fresnel equations. A peak in current is noticeable at 20º, although, comparing this to the simulated absorption plots from the TMM, as shown in Figure 26 (a), this is not expected.

The previous results suggest that the solar cells were not behaving properly. It is a known fact that degradation is a big issue with organic materials in solar cells. Degradation can occur in various ways, e.g.,

exposure to oxygen, humidity, temperature, atmospheric pressure, and long exposures to light. The solar cells in here described were already fabricated a year prior to the start of this thesis and were used in a different project, and by the time they were tested in the Fourier microscopy setup they had already been subjected to multiple degradation factors that might have impacted its functionality. Apart from that, the laser used to make measurements on the cells could have been degrading them. A combination of the reasons mentioned above could cause a non-homogenous surface that will therefore present different J_{SC} values at different parts of the cell.

To understand if the degradation of the cells was affecting the results, the P420 cell was subjected to a test of current decay over time. Here, the Fianium laser was set to shine a λ = 596 nm light beam for 10 minutes at the same position on the cell for normal incidence. The results (Figure 29 (a)) show a decrease in current over time with values that have the same order of magnitude as the J_{SC} plot for the same cell, proving that the cell was prone to degradation throughout the measurements done, even for short periods of time.

To better understand the degradation issues of the cell and its probable lack of homogeneity throughout its surface, another study was made (Figure 2929 (b)). The current provided by the multimeter for the P420 cell was recorded by displacing the sample holder in steps of 14 microns in time steps of 10 seconds (this was done by making a direct measure on the real-time image provided by the real space camera), maintaining the incident light on the cell at normal incidence. A change in the current measurements at different positions of the cell is noticeable, which indicates that the cells are not homogenous.

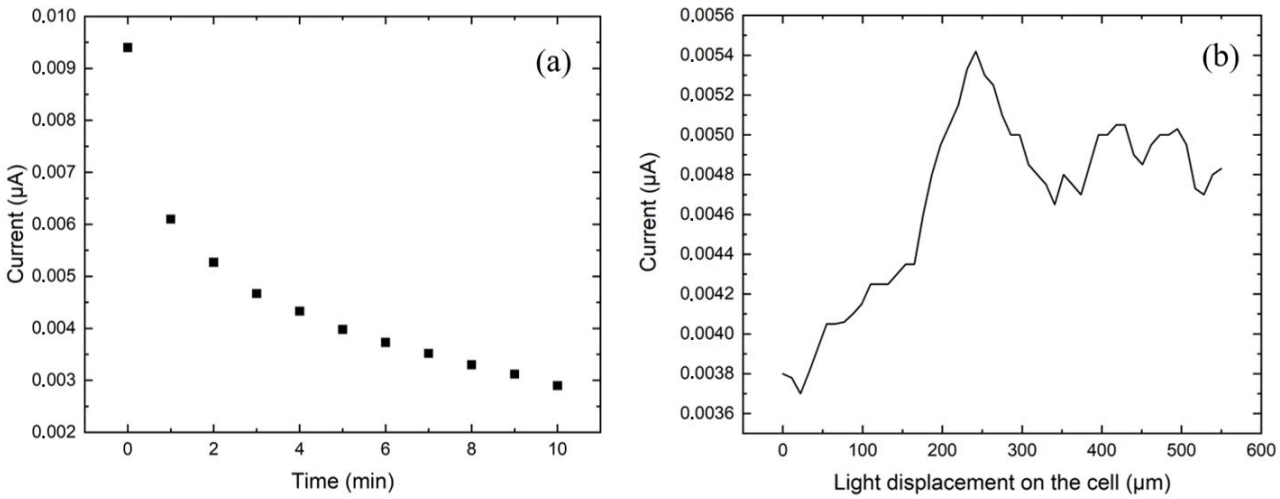

Figure 29 - (a) Current decay over time at normal incidence for the P420 cell; (b) current changes at normal incidence at different positions on the cell.

4

CONCLUSION AND FUTURE PERSPECTIVES

In this work, a Fourier microscope was developed. This setup makes use of the properties of convex lenses to focus an incident light beam on different positions of the back focal plane of an objective lens. This allows the light coming out of the objective to be shifted at a certain range of degrees correlated to the numerical aperture of the objective used. These principles were first introduced and then, the alignment of the setup was described. This alignment, although being simple in paper, is an extensive process of trial and error, as it is for any optical setup. It required a lot of time and attention during the period of this thesis, and different components and configurations were considered until having the best possible alignment.

The setup was used to direct light onto plasmonic solar cells at different (and controllable) incident angles. Simulations of how this change in incident light angle affects the short-circuit current of the cells were done previously to the setup measurements via different simulations software. COMSOL and MATLAB proved to be the most reliable software to do this type of analysis. From those simulations it was foreseen that absorption decreased by increasing the incident light angle (therefore also decreasing the short-circuit current), and thus the initial assumption that the metallic nanoparticles could reverse this decrease at certain wavelengths was discredited. To compare to these results, measurements of the short circuit current of those cells were done using the Fourier microscopy setup. An overall decrease in the short circuit current of those cells was observed for higher angles, however those measurements could not be fully conclusive since it was later proven that the cell had a lack of homogeneity possibly due to degradation factors.

Due to the large number of components required, the setup ended up needing a lot of space – which ultimately adds difficulty on the task of aligning all the components. Therefore, an important consideration to take into account at improving this setup is to limit the amount of space that all the components require – and thus, decrease the path that the light beam needs to travel – to a minimal size. To do this, the best option is to have the lenses of the setup have a smaller focal distance. Another partial solution to improve the setup could be the use of plate or pellicle beam splitters that require less space than the cubic ones used. One could also argue to remove some mirrors for this purpose; although, these mirrors play a big difference on the alignment of the setup since they control the angular and translational displacement of the beam. The use of two mirrors to guide a light beam is a standard procedure in the alignment of optical setups, whereas the first mirror is used to get close to the desired alignment and the second is used to fine tune the alignment on the target. The objective choice should also be considered since it has also been reported in literature that objectives with high numerical aperture and low magnification are the best option for Fourier microscopy, as they grant higher accuracy results [55].

This dissertation was conducted on the Photonics and Semiconductor Nanophysics (PSN) group at the Technical University of Eindhoven (TU/e). The author also contributed to a soon-to-be published article on the Journal of Applied Physics entitled “Evolutionary Optimization of the Short-Circuit Current Enhancement in Organic Solar Cells by Nanostructured Electrodes”, although not entirely related to the work hereby presented.

BIBLIOGRAPHY

[1] S. L. Diedenhofen *et al.*, "Controlling the directional emission of light by periodic arrays of heterostructured semiconductor nanowires," *ACS Nano*, vol. 5, no. 7, pp. 5830–5837, Jul. 2011, doi: 10.1021/NN201557H/ASSET/IMAGES/MEDIUM/NN-2011-01557H_0008.GIF.

[2] S. L. Diedenhofen, O. T. A. Janssen, G. Grzela, E. P. A. M. Bakkers, and J. Gómez Rivas, "Strong geometrical dependence of the absorption of light in arrays of semiconductor nanowires," *ACS Nano*, vol. 5, no. 3, pp. 2316–2323, Mar. 2011, doi: 10.1021/NN103596N/SUPPL_FILE/NN103596N_SI_001.PDF.

[3] I. Gryczynski, J. Malicka, Z. Gryczynski, and J. R. Lakowicz, "Radiative decay engineering 4. Experimental studies of surface plasmon-coupled directional emission," *Anal. Biochem.*, vol. 324, no. 2, p. 170, Jan. 2004, doi: 10.1016/J.AB.2003.09.036.

[4] F. B. Leloup, S. Forment, P. Dutré, M. R. Pointer, and P. Hanselaer, "Design of an instrument for measuring the spectral bidirectional scatter distribution function," *Appl. Opt. Vol. 47, Issue 29, pp. 5454-5467*, vol. 47, no. 29, pp. 5454–5467, Oct. 2008, doi: 10.1364/AO.47.005454.

[5] N. Yu *et al.*, "Small-divergence semiconductor lasers by plasmonic collimation," *Nat. Photonics 2008 29*, vol. 2, no. 9, pp. 564–570, Jul. 2008, doi: 10.1038/nphoton.2008.152.

[6] L. Novotny and B. Hecht, "Principles of nano-optics," *Princ. Nano-Optics*, vol. 9780521832243, pp. 1–539, Jan. 2006, doi: 10.1017/CBO9780511813535.

[7] A. Farré *et al.*, "Optimized back-focal-plane interferometry directly measures forces of optically trapped particles," *Opt. Express, Vol. 20, Issue 11, pp. 12270-12291*, vol. 20, no. 11, pp. 12270–12291, May 2012, doi: 10.1364/OE.20.012270.

[8] M. Yoshita, K. Koyama, M. Baba, and H. Akiyama, "Fourier imaging study of efficient near-field optical coupling in solid immersion fluorescence microscopy," *J. Appl. Phys.*, vol. 92, no. 2, p. 862, Jun. 2002, doi: 10.1063/1.1487442.

[9] J. G. Rivas, G. Vecchi, and V. Giannini, "Surface plasmon polariton-mediated enhancement of the emission of dye molecules on metallic gratings," *New J. Phys.*, vol. 10, no. 10, p. 105007, Oct. 2008, doi: 10.1088/1367-2630/10/10/105007.

[10] A. G. Curto, G. Volpe, T. H. Taminiau, M. P. Kreuzer, R. Quidant, and N. F. Van Hulst, "Unidirectional emission of a quantum dot coupled to a nanoantenna," *Science*, vol. 329, no. 5994, pp. 930–933, Aug. 2010, doi: 10.1126/SCIENCE.1191922.

[11] B. Wang *et al.*, "Fourier microscopy of single plasmonic scatterers," *New J. Phys.*, vol. 13, no. 8, p. 083019, Aug. 2011, doi: 10.1088/1367-2630/13/8/083019.

[12] T. Shegai *et al.*, "Unidirectional broadband light emission from supported plasmonic nanowires," *Nano Lett.*, vol. 11, no. 2, pp. 706–711, Feb. 2011, doi: 10.1021/NL103834Y.

[13] V. Stockhausen, L. Andrade, D. Ivanou, B. Stannowski, and A. Mendes, "Incident Angle and Light Intensity Variation: a Comparative Impact Study on Perovskite, Dye-sensitized and Silicon Heterojunction Solar Cells Towards Building-Integrated Applications," *Sol. Energy Mater. Sol. Cells*, vol. 191, pp. 451–458, 2018, doi: 10.1016/j.solmat.2018.11.020.

[14] G. Makrides *et al.*, "Performance of Photovoltaics Under Actual Operating Conditions," *Third Gener. Photovoltaics*, Mar. 2012, doi: 10.5772/27386.

[15] I. Geisemeyer *et al.*, “Angle dependence of solar cells and modules: The role of cell texturization,” *IEEE J. Photovoltaics*, vol. 7, no. 1, pp. 19–24, Jan. 2017, doi: 10.1109/JPHOTOV.2016.2614120.

[16] R. G. González-Acuña, H. A. Chaparro-Romo, and J. C. Gutiérrez-Vega, “Analytical Lens Design,” *Anal. Lens Des.*, Apr. 2020, doi: 10.1088/978-0-7503-3167-8.

[17] C. Gerhard, “Lens Design Basics,” *Lens Des. Basics*, 2020, doi: 10.1088/978-0-7503-2240-9.

[18] R. Kingslake and R. B. Johnson, “Lens Design Fundamentals,” *Lens Des. Fundam.*, 2010, doi: 10.1016/C2009-0-22069-1.

[19] A. B. Vasista, D. K. Sharma, and P. Kumar, “Fourier plane optical microscopy and spectroscopy,” doi: 10.1002/3527600434.

[20] G. Grzela, “DIRECTIONAL LIGHT EMISSION AND ABSORPTION BY SEMICONDUCTOR NANOWIRES,” Accessed: Oct. 12, 2022. [Online]. Available: http://www.amolf.nl.

[21] “PhD Thesis Heinrich Kirchauer.” https://www.iue.tuwien.ac.at/phd/kirchauer/diss.html (accessed Oct. 12, 2022).

[22] M. Mansuripur, “Classical Optics and its Applications,” *Class. Opt. its Appl. Second Ed.*, vol. 9780521881692, pp. 1–701, Jan. 2009, doi: 10.1017/CBO9780511803796.

[23] P. Biagioni, J. S. Huang, and B. Hecht, “Nanoantennas for visible and infrared radiation,” *Rep. Prog. Phys.*, vol. 75, no. 2, Feb. 2012, doi: 10.1088/0034-4885/75/2/024402.

[24] A. B. Vasista *et al.*, “Differential Wavevector Distribution of Surface-Enhanced Raman Scattering and Fluorescence in a Film-Coupled Plasmonic Nanowire Cavity,” *Nano Lett.*, vol. 18, no. 1, pp. 650–655, Jan. 2018, doi: 10.1021/ACS.NANOLETT.7B05080/SUPPL_FILE/NL7B05080_SI_001.PDF.

[25] T. Ahmad and D. Zhang, “A critical review of comparative global historical energy consumption and future demand: The story told so far,” *Energy Reports*, vol. 6, pp. 1973–1991, Nov. 2020, doi: 10.1016/J.EGYR.2020.07.020.

[26] “Best Research-Cell Efficiency Chart | Photovoltaic Research | NREL.” https://www.nrel.gov/pv/cell-efficiency.html (accessed Oct. 12, 2022).

[27] Y. Huang, E. J. Kramer, A. J. Heeger, and G. C. Bazan, “Bulk heterojunction solar cells: Morphology and performance relationships,” *Chem. Rev.*, vol. 114, no. 14, pp. 7006–7043, Jul. 2014, doi: 10.1021/CR400353V/ASSET/IMAGES/CR400353V.SOCIAL.JPEG_V03.

[28] S. Rafique, S. M. Abdullah, K. Sulaiman, and M. Iwamoto, “Fundamentals of bulk heterojunction organic solar cells: An overview of stability/degradation issues and strategies for improvement,” *Renew. Sustain. Energy Rev.*, vol. 84, pp. 43–53, Mar. 2018, doi: 10.1016/J.RSER.2017.12.008.

[29] M. C. Scharber and N. S. Sariciftci, “Efficiency of bulk-heterojunction organic solar cells,” *Prog. Polym. Sci.*, vol. 38, no. 12, p. 1929, Dec. 2013, doi: 10.1016/J.PROGPOLYMSCI.2013.05.001.

[30] A. J. MouÍ, J. B. Bonekamp, and K. Meerholz, “The effect of active layer thickness and composition on the performance of bulk-heterojunction solar cells,” *J. Appl. Phys.*, vol. 100, no. 9, p. 094503, Nov. 2006, doi: 10.1063/1.2360780.

[31] P. E. Shaw, A. Ruseckas, and I. D. W. Samuel, “Exciton Diffusion Measurements in Poly(3-hexylthiophene),” *Adv. Mater.*, vol. 20, no. 18, pp. 3516–3520, Sep. 2008, doi: 10.1002/ADMA.200800982.

[32] F. Li, L. Kou, W. Chen, C. Wu, and T. Guo, “Enhancing the short-circuit current and power conversion efficiency of polymer solar cells with graphene quantum dots derived from double-walled carbon

nanotubes," *NPG Asia Mater.*, vol. 5, no. 8, Aug. 2013, doi: 10.1038/AM.2013.38.

[33] F. Cheng *et al.*, "Enhancing the short-circuit current and efficiency of organic solar cells using MoO3 and CuPc as buffer layers," *undefined*, vol. 95, no. 10, pp. 2914–2919, Oct. 2011, doi: 10.1016/J.SOLMAT.2011.06.027.

[34] N. K. Elumalai and A. Uddin, "Open circuit voltage of organic solar cells: an in-depth review," *Energy Environ. Sci.*, vol. 9, no. 2, pp. 391–410, Feb. 2016, doi: 10.1039/C5EE02871J.

[35] D. Di Nuzzo *et al.*, "Simultaneous Open-Circuit Voltage Enhancement and Short-Circuit Current Loss in Polymer: Fullerene Solar Cells Correlated by Reduced Quantum Efficiency for Photoinduced Electron Transfer," *Adv. Energy Mater.*, vol. 3, no. 1, pp. 85–94, Jan. 2013, doi: 10.1002/AENM.201200426.

[36] H. Y. Chen *et al.*, "Polymer solar cells with enhanced open-circuit voltage and efficiency," *Nat. Photonics 2009 311*, vol. 3, no. 11, pp. 649–653, Nov. 2009, doi: 10.1038/nphoton.2009.192.

[37] J. Yuan *et al.*, "Single-Junction Organic Solar Cell with over 15% Efficiency Using Fused-Ring Acceptor with Electron-Deficient Core," *Joule*, vol. 3, no. 4, pp. 1140–1151, Apr. 2019, doi: 10.1016/J.JOULE.2019.01.004.

[38] M. Topič *et al.*, "Detailed optical modelling and light-management of thin-film organic solar cells with consideration of small-area effects," *Opt. Express, Vol. 25, Issue 4, pp. A176-A190*, vol. 25, no. 4, pp. A176–A190, Feb. 2017, doi: 10.1364/OE.25.00A176.

[39] H. P. Wang *et al.*, "Photon management in nanostructured solar cells," *J. Mater. Chem. C*, vol. 2, no. 17, pp. 3144–3171, Apr. 2014, doi: 10.1039/C3TC32067G.

[40] A. Raman *et al.*, "Dielectric nanostructures for broadband light trapping in organic solar cells," *Opt. Express, Vol. 19, Issue 20, pp. 19015-19026*, vol. 19, no. 20, pp. 19015–19026, Sep. 2011, doi: 10.1364/OE.19.019015.

[41] K. Yao *et al.*, "Plasmonic Metal Nanoparticles with Core-Bishell Structure for High-Performance Organic and Perovskite Solar Cells," *ACS Nano*, vol. 13, no. 5, pp. 5397–5409, May 2019, doi: 10.1021/ACSNANO.9B00135/SUPPL_FILE/NN9B00135_SI_001.PDF.

[42] L. Qiao *et al.*, "Localized surface plasmon resonance enhanced organic solar cell with gold nanospheres," *Appl. Energy*, vol. 88, pp. 848–852, 2011, doi: 10.1016/j.apenergy.2010.09.021.

[43] J. L. Wu *et al.*, "Surface plasmonic effects of metallic nanoparticles on the performance of polymer bulk heterojunction solar cells," *ACS Nano*, vol. 5, no. 2, pp. 959–967, Feb. 2011, doi: 10.1021/NN102295P.

[44] J. R. Tumbleston, D.-H. Ko, E. T. Samulski, and R. Lopez, "Absorption and quasiguided mode analysis of organic solar cells with photonic crystal photoactive layers," *Opt. Express*, vol. 17, no. 9, p. 7670, Apr. 2009, doi: 10.1364/OE.17.007670.

[45] H. Shen, P. Bienstman, and B. Maes, "Plasmonic absorption enhancement in organic solar cells with thin active layers," *J. Appl. Phys.*, vol. 106, no. 7, p. 073109, Oct. 2009, doi: 10.1063/1.3243163.

[46] C. C. D. Wang *et al.*, "Optical and electrical effects of gold nanoparticles in the active layer of polymer solar cells," *J. Mater. Chem.*, vol. 22, no. 3, pp. 1206–1211, Dec. 2011, doi: 10.1039/C1JM14150C.

[47] M. Notarianni, K. Vernon, A. Chou, M. Aljada, J. Liu, and N. Motta, "Plasmonic effect of gold nanoparticles in organic solar cells," *Sol. Energy*, vol. 106, pp. 23–37, Aug. 2014, doi: 10.1016/J.SOLENER.2013.09.026.

[48] M. Xue *et al.*, "Charge-carrier dynamics in hybrid plasmonic organic solar cells with Ag nanoparticles,"

Appl. Phys. Lett., vol. 98, no. 25, p. 253302, Jun. 2011, doi: 10.1063/1.3601742.

[49] N. Kalfagiannis *et al.*, "Plasmonic silver nanoparticles for improved organic solar cells," *Sol. Energy Mater. Sol. Cells*, vol. 104, pp. 165–174, Sep. 2012, doi: 10.1016/J.SOLMAT.2012.05.018.

[50] B. Wu *et al.*, "Uncovering loss mechanisms in silver nanoparticle-blended plasmonic organic solar cells," *Nat. Commun.*, vol. 4, 2013, doi: 10.1038/NCOMMS3004.

[51] J. Zhu *et al.*, "Plasmonic effects for light concentration in organic photovoltaic thin films induced by hexagonal periodic metallic nanospheres," *Appl. Phys. Lett.*, vol. 98, no. 15, p. 151110, Apr. 2011, doi: 10.1063/1.3577611.

[52] "Angle to Position and Back | David P. Hoffman, PhD." https://david-hoffman.github.io/post/angle-to-position-and-back/ (accessed Oct. 12, 2022).

[53] F. Depasse, M. A. Paesler, D. Courjon, and J. M. Vigoureux, "Huygens-Fresnel principle in the near field," *Opt. Lett.*, vol. 20, no. 3, p. 234, Feb. 1995, doi: 10.1364/OL.20.000234.

[54] Maciej Serda *et al.*, "Strong Light-Matter Coupling in Organic Crystals," *Uniw. śląski*, vol. 7, no. 1, pp. 343–354, Apr. 2022, doi: 10.2/JQUERY.MIN.JS.

[55] R. Zia, M. Jiang, and J. A. Kurvits, "Comparative analysis of imaging configurations and objectives for Fourier microscopy," *JOSA A, Vol. 32, Issue 11, pp. 2082-2092*, vol. 32, no. 11, pp. 2082–2092, Nov. 2015, doi: 10.1364/JOSAA.32.002082.

APPENDIX

A photograph of the Fourier setup is shown in Appendix 1, where all the components are denoted. The objective and sample cannot be seen from this perspective, although they are connected to the vertical arm, below Mirror 3.

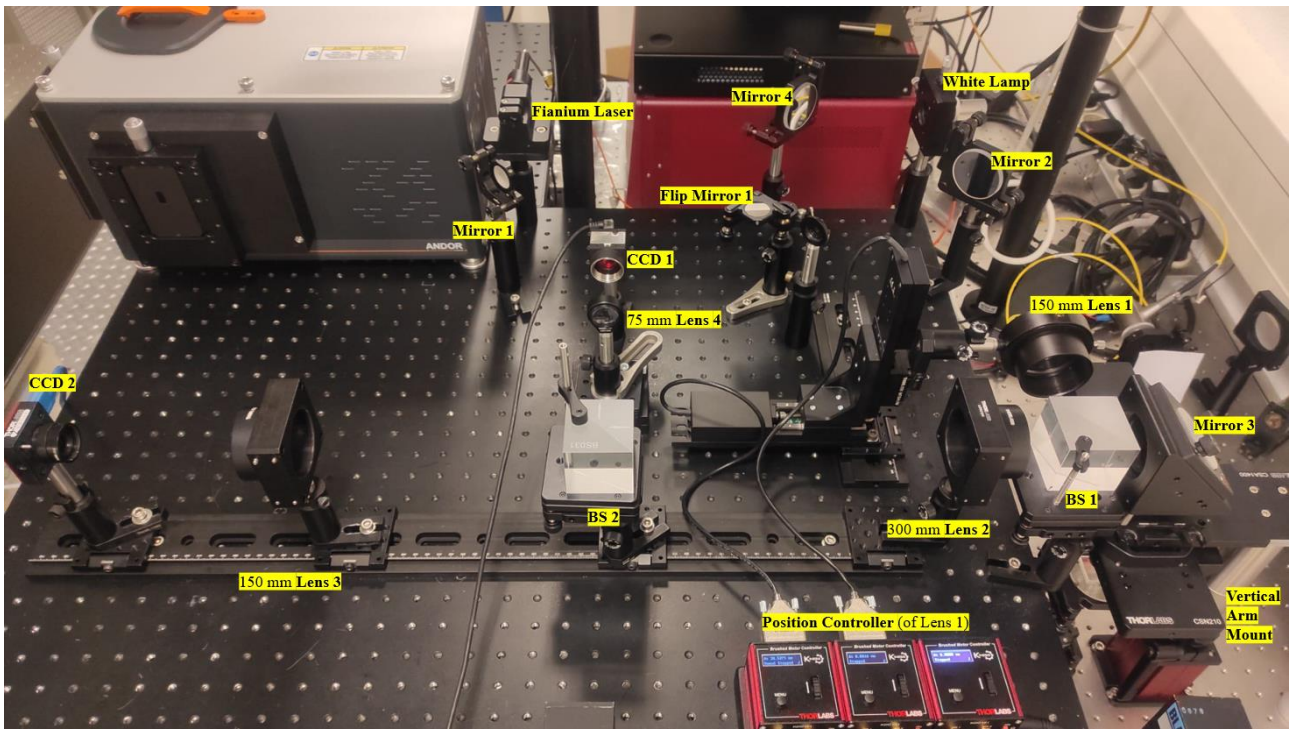

Appendix 1 - Top view of the Fourier microscopy setup built during this thesis.

The bottom table where the vertical arm sits can be seen in Appendix 2, whereas two pinholes are mounted in the vertical arm (seen above Mirror 5). To do measurements with the setup, those two pinholes used for alignment are removed, and an objective and sample holder can be mounted on that same position. In this figure, one can see the Mirror 5 and 405 nm laser, which were used for the alignment of the setup.

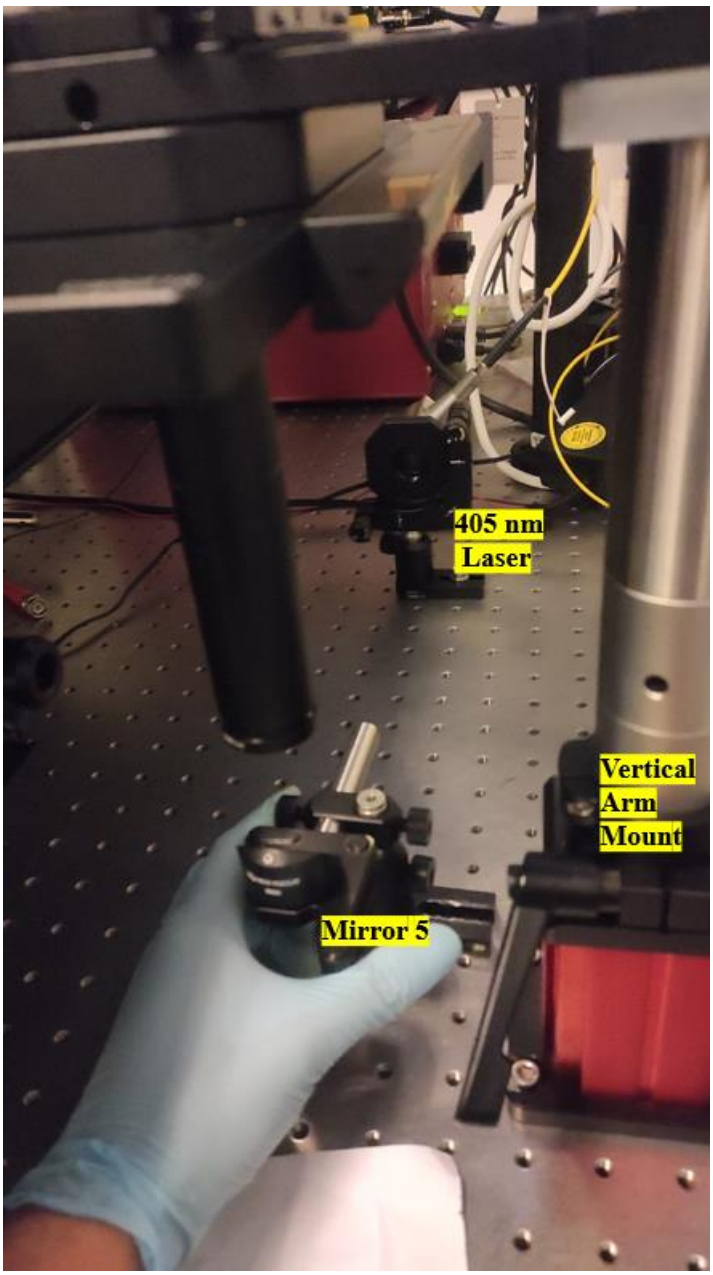

Appendix 2 - Bottom table of the Fourier microscope setup, which was used for the alignment of its components.

On chapter 2.3.2 the alignment of the lenses of the setup was explained, whereas seeing the smallest beam point/size on the CCD cameras meant that the respective lens in front of it was at exactly one focal distance from it. Appendix 3 (a) shows the shape of that spot on the CCD (2) camera while aligning Lens 5, and Appendix 3 (b) represents the same for the alignment of Lens 3. Appendix 3 (c) represents the beam spot seen on the CCD (2) camera, after having Lens 2 and Lens 3 aligned and in place.

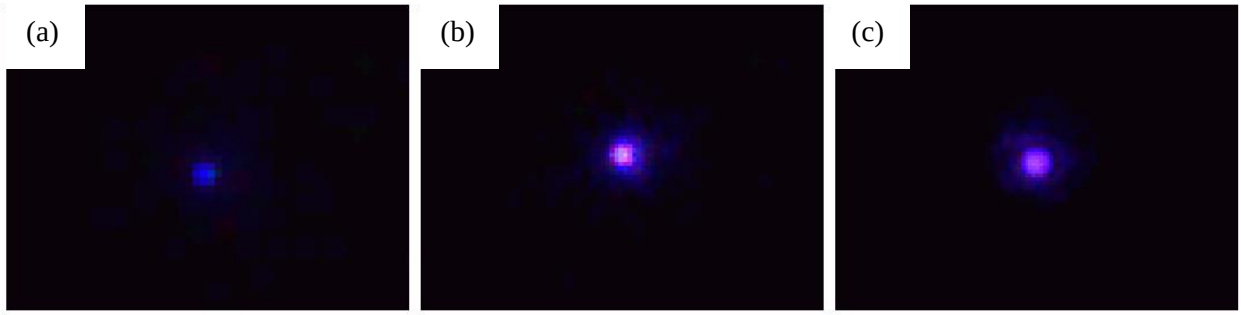

Appendix 3 - Laser shape seen on the CCD 2 camera when aligning the position of (a) Lens 5 and (b) Lens 3. Figure (c) shows the laser spot after aligning both Lens and moving the CCD camera to the focal position of Lens 3.

The EQE box where the solar cells were placed and measured on the Fourier setup can be seen in Appendix 4.

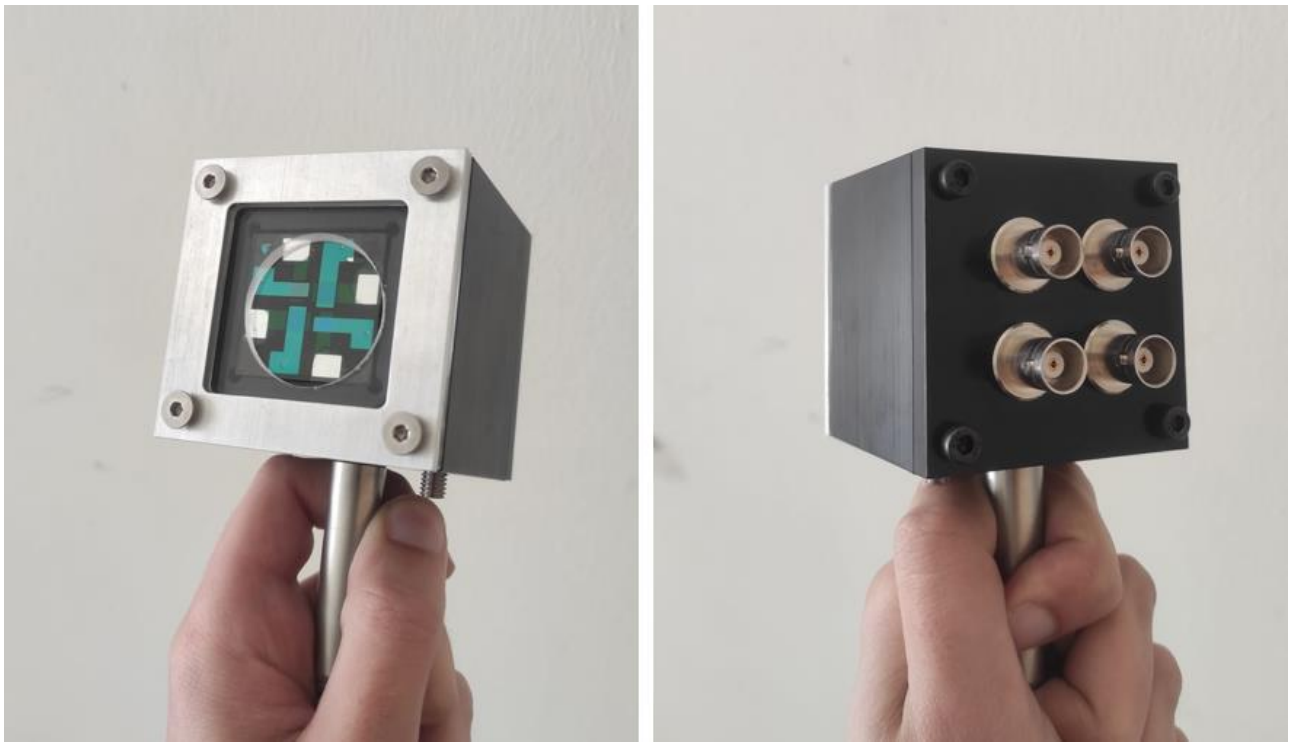

Appendix 4 - EQE box view from the front side (left) and back side (right).